

Discrete Boltzmann multi-scale modelling of non-equilibrium multiphase flows

Yanbiao Gan¹, Aiguo Xu^{2,3,4,†}, Huilin Lai⁵, Wei Li¹, Guanglan Sun^{1,6} and Sauro Succi^{7,8}

¹Hebei Key Laboratory of Trans-Media Aerial Underwater Vehicle, School of Liberal Arts and Sciences, North China Institute of Aerospace Engineering, Langfang 065000, PR China

²Laboratory of Computational Physics, Institute of Applied Physics and Computational Mathematics, PO Box 8009-26, Beijing 100088, PR China

³State Key Laboratory of Explosion Science and Technology, Beijing Institute of Technology, Beijing 100081, PR China

⁴HEDPS, Center for Applied Physics and Technology, and College of Engineering, Peking University, Beijing 100871, PR China

⁵College of Mathematics and Statistics, FJKLMAA, Center for Applied Mathematics of Fujian Province (FJNU), Fujian Normal University, Fuzhou 350117, PR China

⁶School of Physics, Beijing Institute of Technology, Beijing 100081, PR China

⁷Center for Life Nano Science at La Sapienza, Fondazione Istituto Italiano di Tecnologia, Viale Regina Margherita 295, 00161, Roma, Italy

⁸Physics Department and Institute for Applied Computational Science, John A. Paulson School of Applied Science and Engineering, Harvard University, Oxford Street 29, Cambridge, MA 02138, USA

(Received 24 March 2022; revised 19 September 2022; accepted 21 September 2022)

The aim of this paper is twofold: the first aim is to formulate and validate a multi-scale discrete Boltzmann method (DBM) based on density functional kinetic theory for thermal multiphase flow systems, ranging from continuum to transition flow regime; the second aim is to present some new insights into the thermo-hydrodynamic non-equilibrium (THNE) effects in the phase separation process. Methodologically, for bulk flow, DBM includes three main pillars: (i) the determination of the fewest kinetic moment relations, which are required by the description of significant THNE effects beyond the realm of continuum fluid mechanics; (ii) the construction of an appropriate discrete equilibrium distribution function recovering all the desired kinetic moments; (iii) the detection, description, presentation and analysis of THNE based on the moments of the non-equilibrium distribution ($f - f^{(eq)}$). The incorporation of appropriate additional higher-order thermodynamic kinetic moments considerably extends the DBM's capability of handling larger values of the liquid–vapour density ratio, curbing spurious currents, and ensuring mass/momentum/energy conservation. Compared with the DBM with only

† Email address for correspondence: Xu_Aiguo@iapcm.ac.cn

first-order THNE (Gan *et al.*, *Soft Matt.*, vol. 11 (26), 2015, pp. 5336–5345), the model retrieves kinetic moments beyond the third-order super-Burnett level, and is accurate for weak, moderate and strong THNE cases even when the local Knudsen number exceeds 1/3. Physically, the ending point of the linear relation between THNE and the concerned physical parameter provides a distinct criterion to identify whether the system is near or far from equilibrium. Besides, the surface tension suppresses the local THNE around the interface, but expands the THNE range and strengthens the THNE intensity away from the interface through interface smoothing and widening.

Key words: multiphase flow, gas/liquid flows, kinetic theory

1. Introduction

Multiphase flows with phase transitions and heat transfer are ubiquitous in natural and industrial processes, such as atmospheric phenomena, material and food processing, petrochemical engineering and bio-medicine, as well as life sciences (Brennen 2005; Bernaschi, Melchionna & Succi 2019; Zang *et al.* 2019; Wu, Liu & Wang 2021*b*). Therefore, establishing accurate, reliable and efficient models and computational strategies for predicting their flow behaviour will deepen our understanding of the fundamental and underlying physical mechanisms behind multiphase flows. Besides major academic significance as complex phenomena far from equilibrium, they also bear essential industrial value.

Nevertheless, multi-scale modelling and simulation of such a complex system is a long-standing challenge (Luo, Xia & Monaco 2009; Bernaschi *et al.* 2019; Zang *et al.* 2019). The challenge arises from the common and unique features of these fluids: (i) complex multi-scale structures and their cross-scale correlations, such as particles, bubbles, droplets and clusters; (ii) rich and abundant evolving interfaces, such as material and mechanical interfaces; (iii) complex forces, relaxations and responses, such as gradient, interparticle and external forces, and the nonlinear coupling among them; (iv) competition between various spatiotemporal scales and kinetic modes, such as growth, deformation, breakup, cavitation, boiling and even turbulence.

In general, a multiphase flow system is in a global or local thermo-hydrodynamic non-equilibrium (THNE) state with fluctuations (Parsa & Wagner 2020), including significant hydrodynamic and thermodynamic non-equilibrium (HNE and TNE, respectively) effects that may undermine the validity of macroscopic models, such as the most commonly used Navier–Stokes (NS) equations. Simplifying assumptions, such as thermal equilibrium across a liquid–vapour interface during phase separation, can lead to erroneous predictions (Persad & Ward 2016). A possible solution for accessing detailed THNE effects is to use particle-based methods, for example, molecular dynamics or the direct simulation Monte Carlo method (Liu *et al.* 2017, 2020). However, the spatiotemporal scales and geometries that the two schemes can afford are extremely small and highly idealized compared with those of practical applications.

As a mesoscopic approach and a natural bridge connecting microscopic and macroscopic models, suitably extended versions of the Boltzmann equation can in principle describe the complex non-equilibrium thermo-hydrodynamics for the full spectrum of flow regimes (Chapman & Cowling 1990). However, the nonlinearity, multi-dimensionality, and integro-differential nature of the collision term pose a formidable challenge to its direct solution. The difficulty in using the original Boltzmann

equation has prompted the development of approximate and simplified kinetic models that relinquish much of its computational complexity while preserving its most relevant physics in point. The versatile lattice Boltzmann method (LBM) (Benzi, Succi & Vergassola 1992; Chen & Doolen 1998; Wagner & Yeomans 1998; Succi 2001, 2018; Zheng, Shu & Chew 2006; Sbragaglia *et al.* 2007; Xu *et al.* 2012; Guo & Shu 2013; Bernaschi *et al.* 2019; Falcucci *et al.* 2021; Huang *et al.* 2021a; Bhairapurada, Denet & Boivin 2022; Wei *et al.* 2022) and the recently developed discrete Boltzmann method (DBM) (Gan *et al.* 2015, 2018, 2019; Lai *et al.* 2016; Lin *et al.* 2017; Zhang *et al.* 2019, 2021; Chen *et al.* 2020; Xu *et al.* 2021a,b,c) belong precisely to this class of modern non-equilibrium methods.

As for the LBM research, there are two complementary branches. The first is a physics-inspired construction method, while the second is a numerical scheme for solving partial differential equations, such as the wave equation (Yan 2000; Lai & Ma 2011), convection–diffusion equation (Du & Liu 2020; Chen *et al.* 2021b), Poisson equation (Chai & Shi 2008), Laplace equation (Zhang, Yan & Dong 2009), Fisher equation (Succi 2014), Burgers equation (Elton 1996; Duan & Liu 2007; Liu & Shi 2011), Benjamin–Ono equation (Lai & Ma 2010), Korteweg–de Vries equation (Wang 2017b; Lan, Hu & Guo 2019), Klein–Gordon–Zakharov equation (Wang 2019), Zakharov–Kuznetsov equation (Wang 2017a, 2020), Ginzburg–Landau equation (Zhang & Yan 2010, 2014), Kuramoto–Sivashinsky equation (Otomo, Boghosian & Dubois 2018) and Schrödinger equation (Succi 2001; He & Lin 2020). These two branches build on similar, yet not equal, construction rules. The DBM was developed from the first branch and represents a mesoscopic modelling method for fluid flows.

Although the original Boltzmann equation and its approximations work only for dilute gas systems, they can be extended to multiphase flow regimes after incorporating the non-ideal gas effects through a variety of approaches. Actually, both the LBM and the DBM are particularly promising in the area of multiphase and multi-component flows, mainly on account of their kinetic nature, directly inherited from the Boltzmann equation, which facilitates the inclusion of microscopic physical interactions as compared to numerical methods based on continuum models.

To date, many LBMs for multiphase flows have been proposed, including the chromodynamic model Gunstensen *et al.* (1991), the pseudo-potential model (Shan & Chen 1993, 1994), the free-energy model (Swift, Osborn & Yeomans 1995; Swift *et al.* 1996; Xu, Gonnella & Lamura 2003, 2004), the kinetic-theory-based model (He, Shan & Doolen 1998; He, Chen & Zhang 1999), the forcing model (Sofonea *et al.* 2004; Gonnella, Lamura & Sofonea 2007), the phase-field model (Rasin, Miller & Succi 2005), the entropic kinetic model (Mazloomi M, Chikatamarla & Karlin 2015; Montessori *et al.* 2017; Wöhrwag *et al.* 2018) and the unified collision model (Luo, Fei & Wang 2021). Although the models are proposed from different perspectives, their common point is the inclusion of interparticle interactions at the mesoscopic scale. The interparticle interactions are the underlying engine behind the complex THNE features of multiphase flows. The aforementioned models and their revised versions have been applied successfully to the study of fundamental phenomena and mechanisms of multiphase flows in science and engineering, ranging from droplet evaporation (Ledesma-Aguilar, Vella & Yeomans 2014; Safari, Rahimian & Krafczyk 2014; Zarghami & Van den Akker 2017; Qin *et al.* 2019; Fei *et al.* 2022) to droplet deformation, breakup, splashing and coalescence (Wagner, Wilson & Cates 2003; Wang *et al.* 2015a; Wang, Shu & Yang 2015b; Chen & Deng 2017; Wen *et al.* 2017, 2020; Liu *et al.* 2018; Liang *et al.* 2019; Yang *et al.* 2022b), collapsing cavitation (Chen, Zhong & Yuan 2011; Falcucci *et al.* 2013; Kähler *et al.* 2015;

Sofonea *et al.* 2018; Yang *et al.* 2020, 2022a), acoustics levitation (Zang 2020), nucleate boiling (Li *et al.* 2016, 2018; Fei *et al.* 2020), ferrofluid and electro-hydrodynamic flows (Falcucci *et al.* 2009; Hu, Li & Niu 2018; Liu, Chai & Shi 2019), hydrodynamic instability (Zhang *et al.* 2001; Fakhari & Lee 2013; Liang *et al.* 2014, 2016a; Liang, Shi & Chai 2016b; Yang, Zhong & Zhuo 2019; Tavares *et al.* 2021), dendritic growth (Rasin *et al.* 2005; Rojas, Takaki & Ohno 2015; Sun *et al.* 2016a,b), heat and mass transfer in porous media (Chen *et al.* 2015; Chai *et al.* 2016, 2019; Liu *et al.* 2016; He *et al.* 2019), Rayleigh–Bénard convection (Pelusi *et al.* 2021), active fluid (Cates *et al.* 2008; Doostmohammadi *et al.* 2016; Carena *et al.* 2019; Negro *et al.* 2019), isotropic turbulence (Perlekar *et al.* 2014; Milan *et al.* 2020), solid–liquid–vapour phase transition and phase ordering under various conditions (Osborn *et al.* 1995; Gonnella, Orlandini & Yeomans 1997; Corberi, Gonnella & Lamura 1998; Kendon *et al.* 1999; Sofonea *et al.* 2004; Gonnella *et al.* 2010; Coclite, Gonnella & Lamura 2014; Wang *et al.* 2017; Ambruş *et al.* 2019; Busuioc *et al.* 2020; Chen *et al.* 2021c; Huang, Wu & Adams 2021b).

Notwithstanding significant progress, the highly non-equilibrium interfacial thermo-hydrodynamics, which is strongly associated with the growth kinetics and morphological evolution of systems, is seldom reported and still poorly understood. This topic has presented a challenge to the important front of trans-scale modelling and simulation of multiphase flows.

Recently, we have demonstrated that the DBM offers a novel systematic scheme and a set of convenient and efficient tools for describing, measuring and analysing simultaneously THNE effects that cannot be described adequately by traditional hydrodynamic models (Xu *et al.* 2012; Gan *et al.* 2015, 2018; Lai *et al.* 2016; Zhang *et al.* 2019, 2021, 2022a; Chen *et al.* 2020, 2022a; Liu *et al.* 2022). The DBM was developed from a branch of the LBM that aims to describe the non-equilibrium flows from a more fundamental level and is no longer based on the simple ‘propagation + collision’ lattice gas evolution scenario. The key point of the DBM is to ensure that the properties to be studied do not change with model simplification and use the non-conservative kinetic moments of $(f - f^{(0)})$ to describe the system state and extract TNE and THNE information (Xu, Zhang & Zhang 2018a; Xu *et al.* 2021a,b,c), where f is the distribution function, and $f^{(0)}$ is the equilibrium distribution function. Therefore, the simplified Boltzmann-like equation and kinetic moment relations that are not compliant with non-equilibrium statistical physics are prohibited in the DBM. Further, the DBM uses non-conservative kinetic moments of $(f - f^{(0)})$ to open a phase space where the origin corresponds to the thermodynamic equilibrium state, and other points correspond to specific THNE states. The phase space and its subspaces provide a graphic geometric description of non-equilibrium states. Evidently, each non-conservative kinetic moment of $(f - f^{(0)})$ provides its specific contribution to the overall departure from local equilibrium. Hence, as explained above, the choice of the non-equilibrium moments to be retained is dictated by the specific problem at hand.

Methodologically, the DBM belongs to the general framework of non-equilibrium statistical physics, i.e. a specific form of coarse-graining as applied to the physics of fluids beyond the hydrodynamic level. Specifically, the THNE effects presented by the DBM have permitted us to recover the main features of the distribution function (Lin *et al.* 2014; Su & Lin 2022), to capture various interfacial phenomena (Lin *et al.* 2014; Lai *et al.* 2016; Gan *et al.* 2019), to investigate entropy-increasing mechanisms and their relative importance (Zhang *et al.* 2016, 2019), and to clarify some of the fundamental mechanisms of the fine structures of shock waves, contact discontinuities and rarefaction waves beyond

the reach of molecular dynamics (Gan *et al.* 2018; Qiu *et al.* 2020, 2021; Bao *et al.* 2022). Kinetic features, such as the unbalancing and mutual conversion of internal energy at different degrees of freedom, provide appropriate criteria for determining whether or not higher-order TNE effects should be considered in the modelling, and which level of DBM should be adopted (Lin *et al.* 2014; Gan *et al.* 2015, 2018). In plasma physics, kinetic features have been used to distinguish plasma shock wave from shock wave in ordinary neutral flow (Liu *et al.* 2022). These findings and observations shed light on the fundamental mechanisms of various compressible flow systems.

As for the more complicated multiphase case, in 2015, we proposed a DBM with a more realistic equation of state (EOS) to study the HNE and TNE manifestations induced by interparticle and gradient force during phase transition (Gan *et al.* 2015). We found that the maximum of TNE strength can be used as a physical criterion to discriminate the stages of spinodal decomposition and domain growth. In 2019, we further found that the maximum of entropy production rate can be used as another physical criterion to discriminate the two stages (Zhang *et al.* 2019), whereas these models are suitable only for cases with weak non-equilibrium effects, or cases in which the Knudsen number is sufficiently small, including phase separation with a slow quenching rate, shallow quenching depth, limited liquid–vapour density ratio, weak viscous stress and heat flux, but wide interface width.

Two prominent reasons account for the insufficiency of the model far from equilibrium. First, constitutive relations are strictly associated with TNE measures, accounting for the coupling of distinct lengths or time scales, and ultimately determining the accuracy of the hydrodynamic model. Given that few kinetic moments are satisfied by the discrete equilibrium distribution function (DEDF), the model in the previous study (Gan *et al.* 2015) is consistent only with Onuki’s model (Onuki 2005, 2007) for Carnahan–Starling fluid in the hydrodynamic limit with linear constitutive relations, that is, Newton’s law of viscosity and Fourier’s law of heat conduction. Nevertheless, linear constitutive relations result only from the first-order deviation from the thermodynamic equilibrium, and are inadequate for cases with substantial HNE and TNE effects. Second, although higher-order TNE measures and their evolution can be extracted from this DBM (Gan *et al.* 2015), whether or not they are accurate enough should be carefully estimated, preserved and improved.

In this study, we aim to develop a higher-order DBM for the multi-scale modelling of multiphase flow systems ranging from continuum to transition flow regimes. All the inspiring works on higher-order mesoscopic models for non-equilibrium ideal gas flows (Philippi *et al.* 2006; Shan, Yuan & Chen 2006; Zhang, Shan & Chen 2006; Ansumali *et al.* 2007; Chikatamarla & Karlin 2009; Xu 2014; Montessori *et al.* 2015; Ambruş & Sofonea 2016; Coreixas *et al.* 2017; Yang *et al.* 2018; Li, Shi & Shan 2019; He *et al.* 2021; Shi & Shan 2021; Shi, Wu & Shan 2021; Zhang *et al.* 2022a) are out of the scope of the present work, although they can be extended into multiphase flow systems with the approaches listed above. Instead, through Chapman–Enskog multi-scale expansion, we first establish the relationships between TNE measures and the generalized constitutive relations for viscous stress and heat flux beyond the Burnett level; we formulate specific expressions with second-order accuracy for viscous stress, heat flux and other higher-order TNE and THNE quantities that are strictly associated with the evolution of constitutive relations. Moreover, we determine all the fewest required kinetic moments that the DEDF should satisfy, and construct three DBMs for multiphase flows near equilibrium and far from equilibrium by inversely solving the required kinetic moments with efficient discrete velocity models. Finally, we demonstrate theoretically and numerically that the capability of the DBM in describing TNE and THNE effects, as well as its multi-scale

predictive capability, depends on the kinetic moments specifically recovered by the DEDF.

2. DBM for multiphase flows far from equilibrium

In this section, we first reconsider what the original Boltzmann Bhatnagar–Gross–Krook (BGK) model (Bhatnagar, Gross & Krook 1954) describes, and place the BGK model frequently used for various non-equilibrium flows in the proper theoretical perspective for the description of non-dilute systems. Then we focus on the establishment of the links among the Boltzmann–BGK equation, extended hydrodynamic models and THNE phenomena; we determine the necessary kinetic moments to measure THNE effects and discretize phase space using a moment-matching approach. Finally, we present the application of DBMs to multiphase flows far from equilibrium.

2.1. Discrete formulation of density functional kinetic theory

Extended hydrodynamics or generalized hydrodynamics models consider non-equilibrium effects through nonlinear constitutive relations. Correspondingly, high-order kinetic models consider non-equilibrium effects via higher-order distribution functions deviating from equilibrium. As a result, they are expected to be applicable to flows in the slip and transition flow regimes where the NS equations perform poorly (Struchtrup 2005; Gao & Sun 2014). A popular strategy for deriving such models is to perform a Chapman–Enskog multi-scale expansion. In a multiphase system, the starting point is the Boltzmann–BGK equation, supplemented by an appropriate interparticle force (Gonnella *et al.* 2007):

$$\partial_t f + \mathbf{v} \cdot \nabla f = -\frac{1}{\tau} [f - f^{(0)}] + I, \quad (2.1)$$

where $f^{(0)} = (\rho/2\pi T) \exp[-\mathbf{v}^* \cdot \mathbf{v}^*/2T]$ in the two-dimensional case, with ρ , T and \mathbf{v}^* the local density, temperature and thermal velocity, respectively. Here, $\mathbf{v}^* = \mathbf{v} - \mathbf{u}$, with \mathbf{v} the particle velocity, and \mathbf{u} the fluid velocity. Finally, I indicates the kinetic formulation of interparticle force accounting for the non-ideal gas effects.

At this stage, it is important to point out that the original BGK equation (Bhatnagar *et al.* 1954) assumes that the net effect of collisions is to relax the velocity distribution function towards a local equilibrium distribution $f^{(0)}$, over a microscopic velocity-independent characteristic timescale τ . As a result, it describes molecular collisions in an averaged statistical form, with the only constraint of preserving mass/momentum/energy conservation, as well as the H -theorem, to secure convergent evolution towards a local equilibrium. Strictly speaking, the BGK model is valid only close to equilibrium, i.e. $Kn \ll 1$ and $f \simeq f^{(0)}$, thus covering only a very small portion of the full kinetic space.

To study the kinetic behaviour of non-ideal fluids far from equilibrium, one needs to account for interparticle interactions beyond binary collisions, as well as non-equilibrium effects triggered by strong inhomogeneities. This can be achieved by resorting to a mean-field theory formulation (Stanley 1971), or, more precisely, to a density functional kinetic theory (DFKT) (Succi *et al.* 2021). The role of DFKT is twofold: (1) include the effects of the intermolecular interaction potential, omitted by the Boltzmann equation; (2) extend the application scope of the BGK model to non-equilibrium phenomena beyond hydrodynamics. In a pictorial form (see figure 1), one could say that DFKT provides an ‘analytic continuation’ of the BGK model to regions of kinetic phase space not covered by

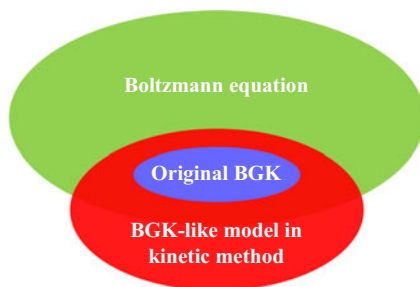


Figure 1. Schematic diagram of the application scopes of the Boltzmann equation, the original BGK model, and a BGK-like model in the kinetic method.

the original Boltzmann equation itself. Here, BGK-like refers to various families of model Boltzmann equations based on single and multi-time relaxation approximations.

In addition, the BGK-like models used widely in the study of complex fluids include several other physical modelling improvements, for example: relaxation times related to local macroscopic quantities (Li & Zhang 2004; Li *et al.* 2015) and collision frequency (Struchtrup 1997); pseudo-equilibrium distribution functions that contain non-equilibrium information (Holway 1966; Shakhov 1968; Shan *et al.* 2006; Gao & Sun 2014; Watari 2016); internal degrees of freedom (Rykov 1975) and even quantum vibrational energy (Wu *et al.* 2021a); and appropriate kinetic boundary conditions (Wagner & Pagonabarraga 2002; Sbragaglia & Succi 2005; Sofonea & Sekerka 2005; Toschi & Succi 2005; Benzi *et al.* 2006; Chikatamarla, Ansumali & Karlin 2006; Chen, Zhang & Zhang 2013). These improved models permit to capture a wider range of Knudsen numbers and a higher degree of non-equilibrium.

The multi-scale multiphase DFKT is expected to contribute to the area of materials science for energy–environment applications (Succi *et al.* 2020) and medical purposes (Xu *et al.* 2018b; Li *et al.* 2022). For instance, it may help us: to understand the non-equilibrium transport processes of multiphase flow in proton exchange membrane fuel cells for obtaining better performance, and lower cost, emission and noise (Chen, Kang & Tao 2021a); to investigate the non-equilibrium nucleate boiling mechanism and design suitable surface structures for enhancing nucleate boiling heat transfer efficiency (Biferale *et al.* 2012; Li *et al.* 2018, 2020; Fei *et al.* 2020); to optimize heat source location (Dai *et al.* 2020) and improve the latent heat thermal energy storage rate (Ren 2019; Tian *et al.* 2022); to conduct mesoscale simulations of blood flow (Dupin, Halliday & Care 2006; Yan *et al.* 2012), and generation, transmission and diffusion of bioaerosols (He *et al.* 2022).

In the present paper, as a specific example of DFKT, the mean-field force I takes the following form for a liquid–vapour system:

$$I = -[A + \mathbf{B} \cdot \mathbf{v}^* + (C + C_q)\mathbf{v}^* \cdot \mathbf{v}^*]f^{(0)}. \quad (2.2)$$

The coefficients in (2.2) are designed so as to recover the thermo-hydrodynamic equations proposed by Onuki (Onuki 2005) by using the following contributions of the force term I to mass, momentum and energy equations at the second order in Knudsen number:

$$\int_{-\infty}^{\infty} I \, d\mathbf{v} = A + 2(C + C_q)T, \quad (2.3)$$

$$\int_{-\infty}^{\infty} I \mathbf{v} \, d\mathbf{v} = -\rho T \mathbf{B}, \tag{2.4}$$

$$\int_{-\infty}^{\infty} I \frac{\mathbf{v} \cdot \mathbf{v}}{2} \, d\mathbf{v} = -2\rho T^2(C + C_q) - \rho T \mathbf{B} \cdot \mathbf{u}. \tag{2.5}$$

As a result, $A = -2(C + C_q)T$, indicates that the forcing term guarantees mass conservation, and $\mathbf{B} = (1/\rho T)[\nabla(P^{CS} - \rho T) + \nabla \cdot \mathbf{A}]$ describes two contributions of I to the fluid momentum. One comes from the difference between the non-ideal gas EOS and the ideal gas EOS, and the other comes from the contribution of density gradient to pressure tensor $\mathbf{A} = K \nabla \rho \nabla \rho - K(\rho \nabla^2 \rho + |\nabla \rho|^2/2)\mathbf{I} - [\rho T \nabla \rho \cdot \nabla(K/T)]\mathbf{I}$, with \mathbf{I} the unit tensor, and K the surface tension coefficient. Here, we choose the Carnahan–Starling EOS (Carnahan & Starling 1969) as the non-ideal one, $P^{CS} = \rho T((1 + \eta + \eta^2 - \eta^3)/(1 - \eta)^3) - a\rho^2$ with $\eta = b\rho/4$, which offers a more accurate representation for hard sphere interactions than the van der Waals EOS. A more realistic EOS, such as the Redlich–Kwong (Redlich & Kwong 1949) or the Peng–Robinson (Peng & Robinson 1976), could be incorporated conveniently into the DBM through modifying the extra force term I for modelling improvement. Here, $C = (1/2\rho T^2)\{(P^{CS} - \rho T)\nabla \cdot \mathbf{u} + \mathbf{A} : \nabla \mathbf{u} + a\rho^2 \nabla \cdot \mathbf{u} + K[-\frac{1}{2}(\nabla \rho \cdot \nabla \rho)\nabla \cdot \mathbf{u} - \rho \nabla \rho \cdot \nabla(\nabla \cdot \mathbf{u}) - \nabla \rho \cdot \nabla \mathbf{u} \cdot \nabla \rho]\}$ represents a partial contribution of I to energy. The term $C_q = (1/2\rho T^2)\nabla \cdot [2q\rho T \nabla T]$ permits us to tune the heat conductivity independently of the dynamic viscosity (non-unit Prandtl number).

Constructing the density, momentum and energy kinetic moments of (2.1) and recomposing the time derivative, results in the following extended hydrodynamics equations:

$$\partial_t \rho + \nabla \cdot (\rho \mathbf{u}) = 0, \tag{2.6}$$

$$\partial_t (\rho \mathbf{u}) + \nabla \cdot (\rho \mathbf{u} \mathbf{u} + \mathbf{\Pi} + \mathbf{\Delta}_2) = 0, \tag{2.7}$$

$$\partial_t e_T + \nabla \cdot [e_T \mathbf{u} + \mathbf{\Pi} \cdot \mathbf{u} + \mathbf{\Delta}_{3,1} + \kappa_2 \nabla T] = 0, \tag{2.8}$$

where $\mathbf{\Pi} = P^{CS}\mathbf{I} + \mathbf{A}$ is the non-viscous stress, $e_T = \rho T - a\rho^2 + K|\nabla \rho|^2/2 + \rho u^2/2$ is the total energy density, and $\kappa_2 = 2\rho Tq$ is an additional heat conductivity originated from C_q and designed to tune the Prandtl number. Also, $\mathbf{\Delta}_2$ and $\mathbf{\Delta}_{3,1}$ are typical non-equilibrium measures related to the generalized constitutive relations.

Without loss of generality, two sets of non-equilibrium measures can be defined (Xu *et al.* 2012; Gan *et al.* 2015):

$$\mathbf{\Delta}_{m,n} = M_{m,n}(f - f^{(0)}) = \int_{-\infty}^{\infty} \left(\frac{1}{2}\right)^{1-\delta_{m,n}} (f^{(1)} + f^{(2)} + \dots) \underbrace{\mathbf{v} \mathbf{v} \dots \mathbf{v}}_n (\mathbf{v} \cdot \mathbf{v})^{(m-n)/2} \, d\mathbf{v}, \tag{2.9}$$

$$\begin{aligned} \mathbf{\Delta}_{m,n}^* &= M_{m,n}^*(f - f^{(0)}) \\ &= \int_{-\infty}^{\infty} \left(\frac{1}{2}\right)^{1-\delta_{m,n}} (f^{(1)} + f^{(2)} + \dots) \underbrace{\mathbf{v}^* \mathbf{v}^* \dots \mathbf{v}^*}_n (\mathbf{v}^* \cdot \mathbf{v}^*)^{(m-n)/2} \, d\mathbf{v}, \end{aligned} \tag{2.10}$$

where $\mathbf{\Delta}_{m,n}$ and $\mathbf{\Delta}_{m,n}^*$ are the m th-order tensors contracted to n th-order ones, and $\delta_{m,n}$ is the Kronecker delta function. Here, $(m - n)/2$ is an integer, and when $m = n$, $\mathbf{\Delta}_{m,n}$ and

$\Delta_{m,n}^*$ are referred to simplistically as Δ_m and Δ_m^* , respectively. Also, $\Delta_{m,n}$ describes the combination effects of HNE and TNE, which are usually called the thermo-hydrodynamic non-equilibrium (THNE) effects, and $\Delta_{m,n}^*$ reflects molecular individualism on top of organized collective motion, describing only the TNE effects; $\Delta_{m,n} - \Delta_{m,n}^*$ depicts the HNE effects, as a supplemental description of macroscopic quantity gradients. Term $M_{m,n}$ ($M_{m,n}^*$) is the non-central (central) kinetic moment, and $f^{(j)}$ represents the j th-order derivation from $f^{(0)}$. The decomposition relations among THNE and TNE measures are derived and displayed in [Appendix A](#):

$$\left. \begin{aligned} \Delta_2 &= \Delta_2^*, \\ \Delta_{3,1} &= \Delta_{3,1}^* + \Delta_2^* \cdot \mathbf{u}, \\ \Delta_3 &= \Delta_3^* + (u_\alpha \Delta_{2\beta\gamma}^* + u_\beta \Delta_{2\alpha\gamma}^* + u_\gamma \Delta_{2\alpha\beta}^*) \mathbf{e}_\alpha \mathbf{e}_\beta \mathbf{e}_\gamma, \\ \Delta_{4,2} &= \Delta_{4,2}^* + \Delta_{3,1}^* \mathbf{u} + \mathbf{u} \Delta_{3,1}^* + \Delta_3^* \cdot \mathbf{u} + \Delta_2^* \cdot \mathbf{u} \mathbf{u} + \mathbf{u} \Delta_2^* \cdot \mathbf{u} + \frac{u^2}{2} \Delta_2^*. \end{aligned} \right\} \quad (2.11)$$

Here, Δ_2^* and $\Delta_{3,1}^*$ are also referred to as the non-organized moment flux (NOMF) and non-organized energy flux (NOEF), respectively. Compared with the NS and Burnett equations, Δ_2^* and $\Delta_{3,1}^*$ correspond to more generalized viscous stress and heat flux, which contain all hierarchical TNE effects induced by $(f - f^{(0)})$, instead of only $f^{(1)}$ at the NS level and $f^{(1)} + f^{(2)}$ at the Burnett level. The links among the Boltzmann equation, the extended hydrodynamic equations and TNE measures have been established so far. Terms Δ_3^* and $\Delta_{4,2}^*$ are the flux of viscous stress and the flux of heat flux, respectively.

However, Δ_2^* and $\Delta_{3,1}^*$ are primarily unknown. To obtain the explicit constitutive relations, we perform Chapman–Enskog expansion on both sides of (2.1) by introducing expansions

$$f = f^{(0)} + f^{(1)} + f^{(2)} + \dots, \quad (2.12)$$

$$\partial_t = \partial_{t_1} + \partial_{t_2} + \dots, \quad (2.13)$$

$$\nabla = \nabla_1, \quad I = I_1, \quad (2.14a,b)$$

where ∂_{t_j} , ∇_j and I_j are j th-order terms in Knudsen number ϵ . Substituting (2.12)–(2.14) into (2.1), and equating terms that have the same orders in ϵ , gives

$$\epsilon^1 : \partial_{t_1} f^{(0)} + \nabla_1 \cdot (f^{(0)} \mathbf{v}) = -\frac{1}{\tau} f^{(1)} + I_1, \quad (2.15)$$

$$\epsilon^2 : \partial_{t_2} f^{(0)} + \partial_{t_1} f^{(1)} + \nabla_1 \cdot (f^{(1)} \mathbf{v}) = -\frac{1}{\tau} f^{(2)}. \quad (2.16)$$

Performing the velocity moments with the collision invariant vector $(1, \mathbf{v}, v^2/2)$ on the two sides of (2.15) leads to the following useful relations between the temporal derivative ∂_{t_1} and the spatial derivative ∇_1 at ϵ^1 level:

$$\partial_{t_1} \rho = -\nabla_1 \cdot (\rho \mathbf{u}), \quad (2.17)$$

$$\partial_{t_1} \mathbf{u} = -T \mathbf{B} - \nabla_1 T - \frac{T}{\rho} \nabla_1 \rho - \mathbf{u} \cdot \nabla_1 \mathbf{u}, \quad (2.18)$$

$$\partial_{t_1} T = -2(C + C_q) T^2 - T \nabla_1 \cdot \mathbf{u} - \mathbf{u} \cdot \nabla_1 T. \quad (2.19)$$

From (2.15), we can obtain $f^{(1)} = -\tau[\partial_{t_1} f^{(0)} + \nabla_1 \cdot (f^{(0)} \mathbf{v}) - I_1]$. Using (2.17)–(2.19), and after some straightforward but rather tedious algebraic manipulation, we acquire the

following relations between thermodynamic forces and fluxes:

$$\mathbf{\Delta}_2^{*(1)} = \int_{-\infty}^{\infty} f^{(1)} \mathbf{v}^* \mathbf{v}^* \, d\mathbf{v} = -\mu[\nabla \mathbf{u} + (\nabla \mathbf{u})^T - I \nabla \cdot \mathbf{u}], \quad (2.20)$$

$$\mathbf{\Delta}_{3,1}^{*(1)} = \int_{-\infty}^{\infty} \frac{1}{2} f^{(1)} \mathbf{v}^* \cdot \mathbf{v}^* \mathbf{v}^* \, d\mathbf{v} = -\kappa_1 \nabla T. \quad (2.21)$$

Equations (2.20) and (2.21) indicate that the first orders of NOMF and NOEF are exactly the viscous stress tensor and the heat flux at the NS level, respectively; $\mu = \rho T \tau$ is the viscosity coefficient, and $\kappa_1 = 2\rho T \tau$ is the heat conductivity. Similarly, we have

$$\mathbf{\Delta}_3^{*(1)} = \int_{-\infty}^{\infty} f^{(1)} \mathbf{v}^* \mathbf{v}^* \mathbf{v}^* \, d\mathbf{v} = -\rho T \tau (\partial_\alpha T \delta_{\beta\gamma} + \partial_\beta T \delta_{\alpha\gamma} + \partial_\gamma T \delta_{\alpha\beta}) \mathbf{e}_\alpha \mathbf{e}_\beta \mathbf{e}_\gamma, \quad (2.22)$$

$$\mathbf{\Delta}_{4,2}^{*(1)} = \int_{-\infty}^{\infty} f^{(1)} \mathbf{v}^* \mathbf{v}^* \frac{\mathbf{v}^* \cdot \mathbf{v}^*}{2} \, d\mathbf{v} = -3\rho T^2 \tau [\nabla \mathbf{u} + (\nabla \mathbf{u})^T - I \nabla \cdot \mathbf{u}]. \quad (2.23)$$

Deeper TNE effects can be accessed by considering the contributions of $f^{(2)}$, and clarifying relations between ∂_{t_2} and ∇_1 at ϵ^2 level according to procedures similar to those listed in (2.17)–(2.19). Specifically, from (2.16), we acquire

$$\begin{aligned} f^{(2)} &= -\tau [\partial_{t_2} f^{(0)} + \partial_{t_1} f^{(1)} + \nabla_1 \cdot (f^{(1)} \mathbf{v})] \\ &= -\tau \partial_{t_2} f^{(0)} + \tau^2 \partial_{t_1}^2 f^{(0)} + \tau^2 \partial_{t_1} [\nabla_1 \cdot (f^{(0)} \mathbf{v})] - \tau^2 \partial_{t_1} I_1 \\ &\quad + \tau^2 \nabla_1 \cdot [\partial_{t_1} f^{(0)} \mathbf{v} + \nabla_1 \cdot (f^{(0)} \mathbf{v} \mathbf{v}) - I_1 \mathbf{v}]. \end{aligned} \quad (2.24)$$

It is clear that $f^{(2)}$ can also be expressed in terms of $f^{(0)}$. As a result, non-conservative non-equilibrium moments can finally resort to those of $f^{(0)}$, which triggers the requirement of the higher-order kinetic moments of $f^{(0)}$. The second-order non-organized moment flux reads

$$\mathbf{\Delta}_2^{*(2)} = \mathbf{M}_2^*(f^{(2)}) = \int_{-\infty}^{\infty} f^{(2)} \mathbf{v}^* \mathbf{v}^* \, d\mathbf{v}. \quad (2.25)$$

To obtain an explicit expression, relations between ∂_{t_2} and ∇_1 at ϵ^2 level should be clarified. Performing the velocity moments with the collision invariant vector $(1, \mathbf{v}, v^2/2)$ on the two sides of (2.16) leads to the following useful relations between the temporal derivative ∂_{t_2} and the spatial derivative ∇_1 at ϵ^2 level:

$$\partial_{t_2} \rho = 0, \quad (2.26)$$

$$\rho \partial_{t_2} \mathbf{u} = -\nabla_1 \cdot \mathbf{\Delta}_2^{(1)}, \quad (2.27)$$

$$\partial_{t_2} (\rho T + \frac{1}{2} \rho u^2) = -\nabla_1 \cdot \mathbf{\Delta}_{3,1}^{(1)}. \quad (2.28)$$

Using (2.26)–(2.28) to replace the temporal derivative ∂_{t_2} by spatial derivative ∇_1 at ϵ^2 level, and after some laborious algebraic manipulation, we acquire expression for $\mathbf{\Delta}_2^{*(2)}$. Likewise, analytical expressions for $\mathbf{\Delta}_{3,1}^{*(2)}$, $\mathbf{\Delta}_3^{*(2)}$ and $\mathbf{\Delta}_{4,2}^{*(2)}$ can be obtained, as illustrated in Appendix B. The derivation of these expressions is a tough task, so we resort to the software Maple 18.

Furthermore, multiplying (2.1) by $\mathbf{v}^* \mathbf{v}^*$ and $\frac{1}{2} \mathbf{v}^* \cdot \mathbf{v}^* \mathbf{v}^*$, and integrating over the whole velocity space, we obtain the time-evolution equations for viscous stress and heat flux:

$$\partial_t \Delta_2^* + \partial_t M_2^*(f^{(0)}) + \nabla \cdot [M_3^*(f^{(0)}) + M_2^*(f^{(0)})\mathbf{u} + \Delta_3^* + \Delta_2^*\mathbf{u}] = -\frac{1}{\tau} \Delta_2^* + M_2^*(I), \tag{2.29}$$

$$\begin{aligned} \partial_t \Delta_{3,1}^* + \partial_t M_{3,1}^*(f^{(0)}) + \nabla \cdot [M_{4,2}^*(f^{(0)}) + M_{3,1}^*(f^{(0)})\mathbf{u} + \Delta_{4,2}^* + \Delta_{3,1}^*\mathbf{u}] \\ = -\frac{1}{\tau} \Delta_{3,1}^* + M_{3,1}^*(I). \end{aligned} \tag{2.30}$$

Equations (2.29) and (2.30) suggest that obtaining the expressions of higher-order TNE quantities, such as Δ_3^* and $\Delta_{4,2}^*$, enhances our understanding of the evolution mechanisms of nonlinear constitutive relations.

To summarize, higher-order constitutive relations of second-order accuracy for viscous stress and heat transfer can be formulated as $\Delta_2^* = \Delta_2^{*(1)} + \Delta_2^{*(2)}$, $\Delta_{3,1}^* = \Delta_{3,1}^{*(1)} + \Delta_{3,1}^{*(2)}$, which are expected to noticeably improve the macroscopic modelling. Meanwhile, higher-order TNE measures with second-order accuracy, $\Delta_3^* = \Delta_3^{*(1)} + \Delta_3^{*(2)}$, $\Delta_{4,2}^* = \Delta_{4,2}^{*(1)} + \Delta_{4,2}^{*(2)}$, offer more abundant non-equilibrium scenarios from different aspects and are useful in elucidating the evolutions of higher-order constitutive relations.

In fact, the theoretical expressions of Δ_3^* and $\Delta_{4,2}^*$ are also constitutive relations, which are omitted in the NS equations. In the case of quasi-continuous and near-equilibrium, it is not a big problem if they are omitted. However, as the degree of discretization and thermodynamic non-equilibrium increase, ignoring Δ_3^* and $\Delta_{4,2}^*$ leads to substantial errors. Furthermore, the analytical expressions for THNE with second-order accuracy, $\Delta_2 = \Delta_2^{(1)} + \Delta_2^{(2)}$, $\Delta_{3,1} = \Delta_{3,1}^{(1)} + \Delta_{3,1}^{(2)}$, $\Delta_3 = \Delta_{3,1}^{(1)} + \Delta_{3,1}^{(2)}$ and $\Delta_{4,2} = \Delta_{4,2}^{(1)} + \Delta_{4,2}^{(2)}$, can be acquired from (2.11).

2.2. Discretization of particle velocity space

The velocity space discretization is a critical step in DBM modelling. The above expressions for TNE measures (see Appendix B) have been derived from (2.1) with a continuous equilibrium distribution function $f^{(0)}$. To conduct numerical simulation, it is required to construct a discrete velocity model (DVM) \mathbf{v}_i to discretize the particle velocity space, and formulate the DEDF $f_i^{(0)}$ satisfying all the needed kinetic moments, where $i = 1, 2, 3, \dots, N$, with N the total number of discrete velocities. Chapman–Enskog analysis demonstrates that $f_i^{(0)}$ should satisfy the seven kinetic moments (Gan *et al.* 2015) $M_0, M_1, M_{2,0}, M_2, M_{3,1}, M_3, M_{4,2}$ in the recovery of the targeted hydrodynamic equations at the NS level. In cases with fixed specific heat ratio, $M_0, M_1, M_2, M_3, M_{4,2}$ are independent. In the recovery of the targeted hydrodynamic equations at the Burnett level, $f_i^{(0)}$ should further satisfy M_4 and $M_{5,3}$ (Gan *et al.* 2018). In the recovery of the targeted hydrodynamic equations beyond the Burnett level and description of all the TNE measures displayed in Appendix B with second-order accuracy, $f_i^{(0)}$ should satisfy more higher-order non-equilibrium moments, as listed in table 1. Among them, $M_0, M_1, M_2, M_3, M_4, M_5, M_{6,4}$ and $M_{7,3}$ are independent (see Appendix C).

TNE	Required higher-order kinetic moments			
$\Delta_3^{*(1)}$	M_4	M_5		
$\Delta_{3,1}^{*(1)}$	$M_{5,1}$			
$\Delta_{4,2}^{(1)}$	$M_{5,3}$	$M_{6,2}$		
$\Delta_2^{*(2)}$	M_4	$M_{5,3}$		
$\Delta_3^{*(2)}$	M_4	M_5	$M_{5,3}$	$M_{6,4}$
$\Delta_{3,1}^{*(2)}$	$M_{5,1}$	$M_{5,3}$	$M_{6,2}$	
$\Delta_{4,2}^{*(2)}$	$M_{5,3}$	$M_{6,2}$	$M_{6,4}$	$M_{7,3}$

Table 1. Higher-order kinetic moment relations required for deriving the analytical expressions of TNE measures, where the blue terms are independent constraint relations.

Here, ‘satisfy’ means that the required kinetic moments of $f_i^{(0)}$, originally in integral form, can be calculated in discrete summation form

$$\Phi_n(f^{(0)}) = \int_{-\infty}^{\infty} f^{(0)} \Psi \, dv = \sum_i f_i^{(0)} \Psi_i, \tag{2.31}$$

with $\Psi = [1, v, vv, vvv, vvvv, vvvvv, \frac{1}{2}v \cdot vvvvv, \frac{1}{2}(v \cdot v)^2 vvv]^T$. Equation (2.31) can be rewritten in matrix form as

$$\Phi_n = \Psi \cdot f^{(0)}, \tag{2.32}$$

where $\Phi_n = (M_0, M_1, M_2, M_3, M_4, M_5, M_{6,4}, M_{7,3})^T = (M_0, M_{1x}, M_{1y}, \dots, M_{7,3yyy})^T$ is the set of moments of $f^{(0)}$. Also, $f^{(0)} = (f_1^{(0)}, f_2^{(0)}, \dots, f_{30}^{(0)})^T$ and $\Psi = (C_1, C_2, \dots, C_{30})$ is a 30×30 matrix bridging the DEDF and the kinetic moments with $C_i = (1, v_{ix}, v_{iy}, \dots, \frac{1}{2}v^4 v_{ix}^3, \frac{1}{2}v^4 v_{ix}^2 v_{iy}, \frac{1}{2}v^4 v_{ix} v_{iy}^2, \frac{1}{2}v^4 v_{iy}^3)^T$. Naturally, $f^{(0)}$ can be calculated as (Gan *et al.* 2013)

$$f^{(0)} = \Psi^{-1} \cdot \Phi_n, \tag{2.33}$$

where Ψ^{-1} is the inverse matrix of Ψ . Here, a two-dimensional DVM with 30 discrete velocities, drawn in schematically figure 2, is used to discretize the velocity space and to ensure the existence of Ψ^{-1} :

$$(v_{ix}, v_{iy}) = \begin{cases} \text{cyc} : c(\pm 1, 0) & \text{for } 1 \leq i \leq 4, \\ c(\pm 1, \pm 1) & \text{for } 5 \leq i \leq 8, \\ \text{cyc} : 2c(\pm 1, 0) & \text{for } 9 \leq i \leq 12, \\ 2c(\pm 1, \pm 1) & \text{for } 13 \leq i \leq 16, \\ \text{cyc} : 3c(\pm 1, 0) & \text{for } 17 \leq i \leq 20, \\ 3c(\pm 1, \pm 1) & \text{for } 21 \leq i \leq 24, \\ c(3, 1), c(1, 3) & \text{for } i = 25, 26, \\ c(-2, 1), c(-3, -2) & \text{for } i = 27, 28 \\ c(-1, -2), c(2, -1) & \text{for } i = 29, 30, \end{cases} \tag{2.34}$$

where ‘cyc’ indicates cyclic permutation. The selection of v_{25}, \dots, v_{30} is highly flexible and thus guarantees the existence of Ψ^{-1} and optimizes the stability of the model. Then the discrete coarse-grained evolution equation reads

$$\partial_t f_i + v_i \cdot \nabla f_i = -\frac{1}{\tau} [f_i - f_i^{(0)}] + I_i. \tag{2.35}$$

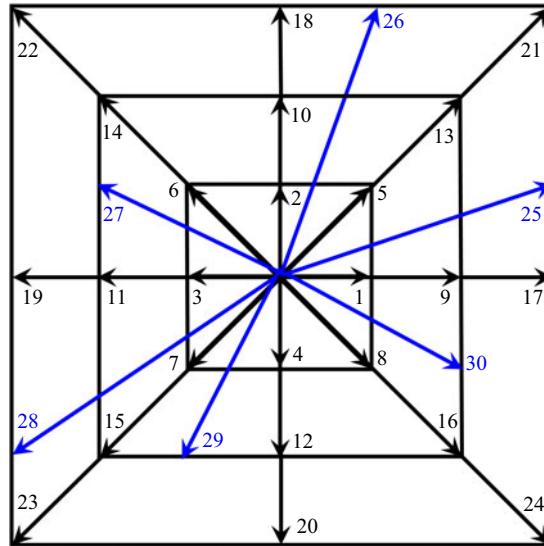


Figure 2. Schematic of the D2V30 discrete velocity model, where v_1, v_2, \dots, v_{24} are symmetric vectors, and $v_{25}, v_{26}, \dots, v_{30}$ are non-symmetric ones, designed to guarantee the existence of Ψ^{-1} .

It is necessary to point out the following.

- (i) The most important step in DBM modelling and simulation is the calculation of $f_i^{(0)}$. The Maxwell distribution satisfies an infinite number of moment relations. Requiring $f_i^{(0)}$ to satisfy all the moment relations is impractical. Which moment relations are necessary depends on the kinetic properties to be studied, a choice that is typically dictated by the intensity of the non-equilibrium effects to be described.
- (ii) The capability of describing non-equilibrium effects relies on the kinetic moment relations that the DBM retrieved correctly. Therefore, by satisfying different kinetic moments, we can systematically construct DBMs for TNE effects at various levels that correspond to different coarse-grained models and own different application ranges. For instance, besides the D2V30 DBM, we propose D2V13, D2V15 and D2V16 multiphase models, and examine their performances in the subsequent section. Here, the D2V13 (D2V15) model adopts the former 13 (15) discrete velocities of the D2V30 model. The D2V16 model indicates the one proposed in (Gan *et al.* 2013) for compressible flows with a flexible specific heat ratio. While considering only the translational degrees of freedom, the D2V16 model will degenerate into the D2V13 model. Independent kinetic moments retrieved by these models are exhibited in table 2.
- (iii) For the same set of grids, the computational cost of the model is proportional to the number of discrete velocities. So, theoretically, the computational cost of the D2V30 model is twice that of the D2V15 model. Compared with the standard multiphase lattice Boltzmann model, such as the well-known Shan–Chen D2Q9 model (Wang *et al.* 2009), the computational cost of the D2V30 model is about 4.4 times that of the D2Q9 model, greater than the ratio of the number of discrete velocities of the two DVMs, 30/9. This originates from the more concise external force term of the Shan–Chen model.

- (iv) The complexity of corresponding hydrodynamic equations increases sharply with the degree of TNE, whereas that of the DBM does not have a significant increase. We can formulate the DBM with the desired order of accuracy by incorporating more needed kinetic moments into Φ_n , and perform simulations without knowing the exact form of the hydrodynamic equations. For example, the D2V30 model satisfies 8 moment relations listed in table 2, and describes viscous stress and heat flux with third-order accuracy. If one wants to achieve fourth-order accuracy, then the physical model needs to further satisfy higher-order moment relations M_6 and $M_{7.5}$. Then the independent ones are M_0 , M_1 , M_2 , M_3 , M_4 , M_5 , M_6 and $M_{7.5}$. For a two-dimensional case, these moment relations have 34 independent components, so a D2V34 model is sufficient to discretize the phase space. Compared with the D2V30 model, the computational cost of the D2V34 model is increased by only 13.33 %.
- (v) The Chapman–Enskog expansion acts as a bridge between the kinetic description given by the DBM and continuum mechanics non-conserved macroscopic dissipation and the conserved variables. Through it, we can determine directly and strictly the minimal physical requirements, and confirm the invariable moment sets Φ_n for modelling a given non-equilibrium state. We also point out that from the perspective of perturbation theory, conducting Chapman–Enskog multi-scale analysis corresponds to imposing a disturbance on the equilibrium system. The convergence of Chapman–Enskog multi-scale expansion corresponds to the system returning to its equilibrium state. If the disturbance is too strong, such as due to the emergence of very steep gradients, leading to the divergence of the Taylor expansion of the distribution function, then the disturbance may trigger new structures or modes, and the Chapman–Enskog analysis fails. Fortunately, in the multiphase flow system, due to the existence of the interface with a certain width, the gradient of the macroscopic quantity is more gentle than that in the high-speed compressible single-phase system, especially in the low-speed multiphase flow with large surface tension.
- (vi) Strictly speaking, the discretization of continuous space inevitably brings non-physical symmetry breaking, and is a source of physical and numerical inaccuracies in the description of the system. Coarse-grained physical modelling is inherently a trade-off. The properties to be studied must be preserved during model simplification, beyond scope of the given study can be sacrificed. Of the many options available to meet the research needs of the current problem, the simplest or most economical is often the first choice. The moment matching approach, shown in (2.31), affords the minimal discrete velocity sets for solving Φ_n , because the number of discrete velocities just equals the number of independent kinetic moment relations. Therefore, physically, the DBM proposed in this way features the highest computational efficiency. These outstanding advantages make the DBM a particularly appealing methodology for investigating non-equilibrium flows. We can also build a more symmetrical DVM by increasing the number of discrete velocities. For example, we can construct a DVM through Hermite expansion (Shan *et al.* 2006; Zhang *et al.* 2006; Gan *et al.* 2008; Li *et al.* 2019; Shi *et al.* 2021) so that the DVM has better spatial symmetry at the cost of increasing the number of discrete velocities. In this paper, we have chosen the simplest form matching the relevant physical constraints for the problems at hand.
- (vii) For bulk flow far from the boundary, the DBM includes three main pillars, described in the Abstract. For near-wall flow, the mechanism for THNE may be greatly

DVMs	Satisfied independent kinetic moments
D2V13	$M_0, M_1, M_2, M_3, M_{4,2}$
D2V15	$M_0, M_1, M_2, M_3, M_{4,2}, M_{5,1}$
D2V16	$M_0, M_1, M_{2,0}, M_2, M_{3,1}, M_3, M_{4,2}$
D2V30	$M_0, M_1, M_2, M_3, M_4, M_5, M_{6,4}, M_{7,3}$

Table 2. Discrete-velocity models and corresponding independent kinetic moments.

different from that for bulk flow, and consequently, a fourth pillar, construction of kinetic boundary conditions, is necessary. A DBM for slip flow is referred to in Zhang *et al.* (2022b).

- (viii) The present work belongs to the category of single-component miscible multiphase flow. There are several works on DBM modelling and simulation of multi-component miscible fluid flows (Lin *et al.* 2016, 2017, 2021; Zhang *et al.* 2020). The extension of the present work to a multi-component immiscible fluid system is currently under consideration. For multi-component immiscible fluid flows, self-aggregation still occurs between different phases, and surface tension still exists between different components. The core of DBM modelling for immiscible multiphase flow is the incorporation of (a) intermolecular interaction in the same component, and (b) intermolecular interaction between different components.

3. Numerical simulations and analysis

In this section, we first validate DBMs at various levels via three benchmarks related to the equilibrium properties in bulk regions. We then evaluate carefully the multi-scale predictive capability of the DBMs by investigating THNE features around the liquid–vapour interface. Finally, we study the effects of relaxation time and surface tension coefficient on thermal phase separation from the non-equilibrium aspects. In all simulations, we set $a = 2$ and $b = 0.4$; then the critical density and temperature are $\rho^c = 1.30444$ and $T^c = 1.88657$, respectively. To improve the numerical stability and accuracy, the windowed fast Fourier transform (FFT) scheme with 16th-order precision (Gan *et al.* 2011, 2012b, 2015) is utilized to discretize the spatial derivatives, and the second-order Runge–Kutta scheme is used to calculate the temporal derivative. Notably, the periodic boundary condition is imposed inherently in the x and y directions because of the adoption of the FFT scheme. For a system with non-periodic boundary conditions, the FFT scheme can also be applied as long as the mirror operation is performed on the non-periodic boundary (Gan *et al.* 2012a), at the cost of doubling the calculation amount. All the parameters used here are dimensionless. Please refer to Zhang *et al.* (2019) for recovery of the actual physical quantities from the numerical results.

3.1. Verification and validation

3.1.1. Liquid–vapour coexistence curve

Here, the liquid–vapour coexistence curve test is used to check if the newly constructed DBMs can reproduce the correct equilibrium thermodynamics of the Carnahan–Starling system. For the problem considered, the initial conditions are $(\rho, T, u_x, u_y) = (\rho_l, 1.82, 0.0, 0.0)$ if $N_x/4 < x \leq 3N_x/4$, otherwise $(\rho, T, u_x, u_y) = (\rho_v, 1.82, 0.0, 0.0)$, where $\rho_l = 1.9643$ and $\rho_v = 0.7569$ are the theoretical liquid and vapour coexisting

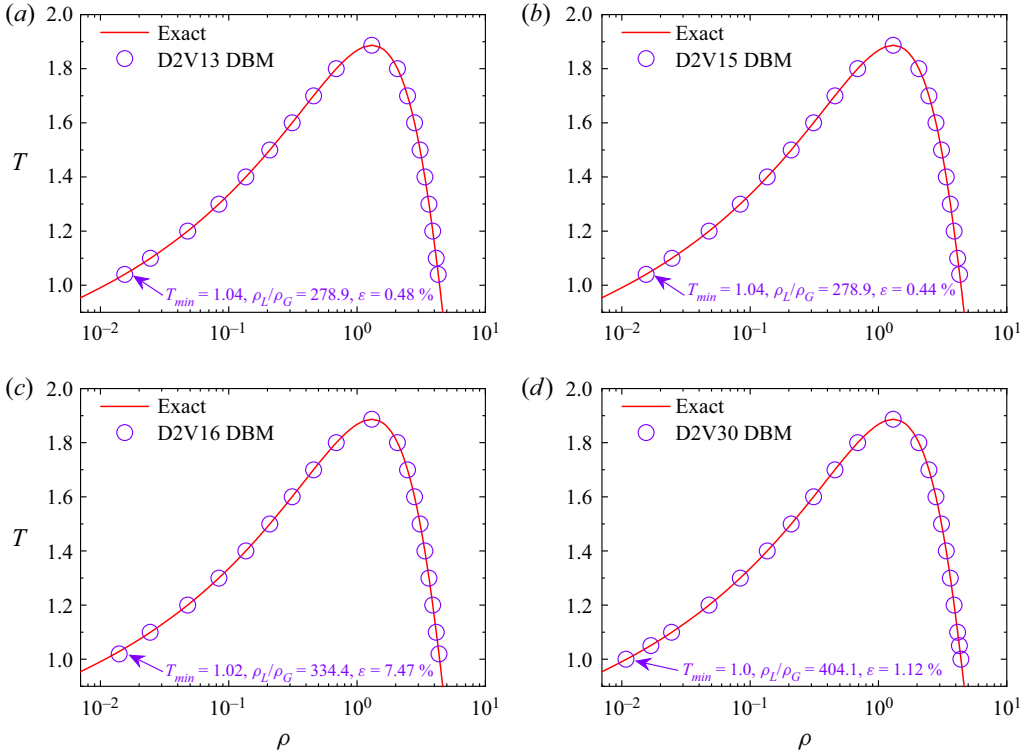


Figure 3. Comparisons of the coexisting densities predicted by various DBMs and Maxwell construction.

densities at $T = 1.82$. Parameters are $\tau = 10^{-4}$, $K = 1.5 \times 10^{-4}$, $\text{Pr} = 0.01$, $N_x \times N_y = 128 \times 1$, $c = 1.25$, $\Delta t = 3 \times 10^{-5}$ and $\Delta x = \Delta y = 4 \times 10^{-3}$ for the D2V13, D2V15 and D2V30 models. But in the D2V16 model, the minimum spatial step that stabilizes the simulation is $\Delta x = \Delta y = 5 \times 10^{-3}$. The initial temperature drops by 0.01 when a steady state has been reached, i.e. $|(u_x^2 + u_y^2)^{1/2}|_{\max} < 10^{-6}$. Figure 3 displays the phase diagrams calculated from the DBM simulations and Maxwell construction. In each panel, the two sets of results are in good agreement with each other. However, the maximum density ratio $R_{\max} = \rho_{\max}/\rho_{\min}$ and the lowest reduced temperature $Tr_{\min} = T_{\min}/T^C$ that each model can undergo are quite different.

The more the moment relations maintained by the DBM, the larger the maximum density ratio and the lower the minimum reduced temperature that the model can attain. Specifically, in the D2V13 model, $R_{\max} = 278.9$ with the maximum relative error in density $\epsilon = |\rho_{\text{DBM}} - \rho_{\text{Exact}}|/\rho_{\text{Exact}} = 0.48\%$ in the vapour branch ($\epsilon_{\max} = 0.28\%$ for the D2V30 model under the same density ratio), whereas in the D2V30 model, R_{\max} can reach up to 404.1 and Tr_{\min} reduces to 0.53 with $\epsilon = 1.12\%$ in the vapour branch.

There are several reasons that account for the fact that the incorporation of higher-order kinetic moments improves the density ratio that the model can sustain. First, physically, the incorporation of higher-order moment relations makes the DBM model more approximate to the continuous Boltzmann–BGK equation with an external force term; that is, the model is more physical. Second, the incorporation of higher-order moment relations makes the DBM more accurate in describing non-equilibrium effects, which greatly affects the computational accuracy and stability, as shown in figure 11. Third, the

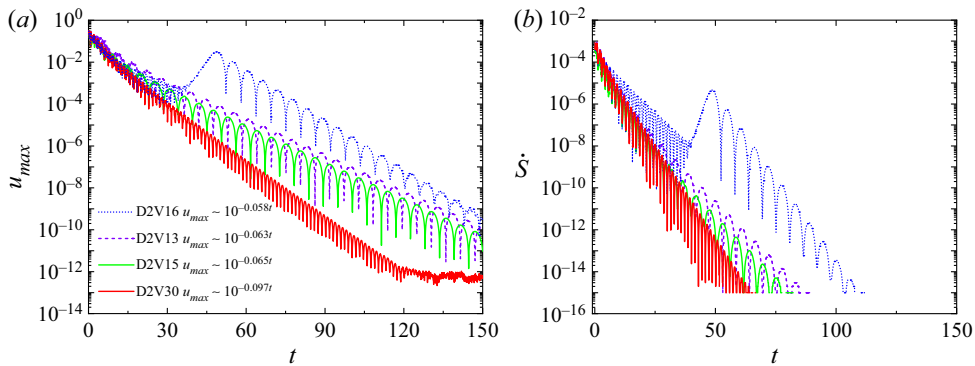


Figure 4. (a) Time evolutions of the maximum velocity u_{max} calculated from various DBMs. (b) Time evolutions of the entropy increase rate.

higher-order model is more capable of ensuring the positive entropy increase rate during the evolution process, with the entropy growth rate defined as (Zhang *et al.* 2019) $dS/dt = \int (\Delta_{3,1}^* \cdot \nabla(1/T) - (1/T)\Delta_2^* : \nabla \mathbf{u}) dr$. Fourth, the incorporation of higher-order moment relations is equivalent to adopting more discrete velocities to discretize the phase space. As the number of discrete velocities increases, the fluctuations of distribution function δf and the spatial gradient of distribution function ∇f decrease, which makes the higher-order model more stable. Lots of numerical examples suggest that the stability improvement of the higher-order model compared to lower-order ones is effective not only for static (or quasi-static) tests, but also for dynamic cases.

3.1.2. Spurious velocity

Figure 4 illustrates the time evolutions of the maximum velocity u_{max} for an initially non-equilibrium planar interface, obtained from various DBM simulations performed using the procedure and parameters exhibited in figure 3, except that the initial temperature is suddenly quenched from 1.45 to 1.10, and the relaxation time is $\tau = 2 \times 10^{-4}$. The spurious velocity, located mainly around the liquid–vapour interface, refers to the residual velocity, which cannot be further reduced after a long period of evolution (Wagner 2003). Specifically, for the D2V30 model, spurious velocity refers to the remaining current when $t > 120$ in figure 4. The decay before $t < 120$ is a physical process decided by the initial condition.

Discarding the early-time transient regime and the very-late-time regime, where u_{max} stays almost unchanged, we find that u_{max} decreases with time t approximately as $u_{max} \sim 10^{-\gamma t}$. But the exponent of the D2V30 model ($\gamma \simeq 0.1$) is considerably larger than that of other models ($\gamma \sim 0.061 \pm 0.003$). When $t > 120.0$, u_{max} decays to a negligible value 10^{-12} in the D2V30 simulation under the combined effects of NOMF and NOEF. Figure 4(b) shows time evolutions of entropy increase rate for the decaying process. When the system temperature is fixed, the entropy increase rate reduces to $dS/dt = - \int (1/T)\Delta_2^* : \nabla \mathbf{u} dr$. The slope of the entropy increase rate reflects the speed at which the system tends towards equilibrium, which is qualitatively consistent with figure 4(a). The larger the slope of the entropy increase rate, the faster the decay in u_{max} . Compared with lower-order models, a faster decay in u_{max} obtained from the D2V30 model is due to a more accurate viscous stress that the model recovers. These findings suggest

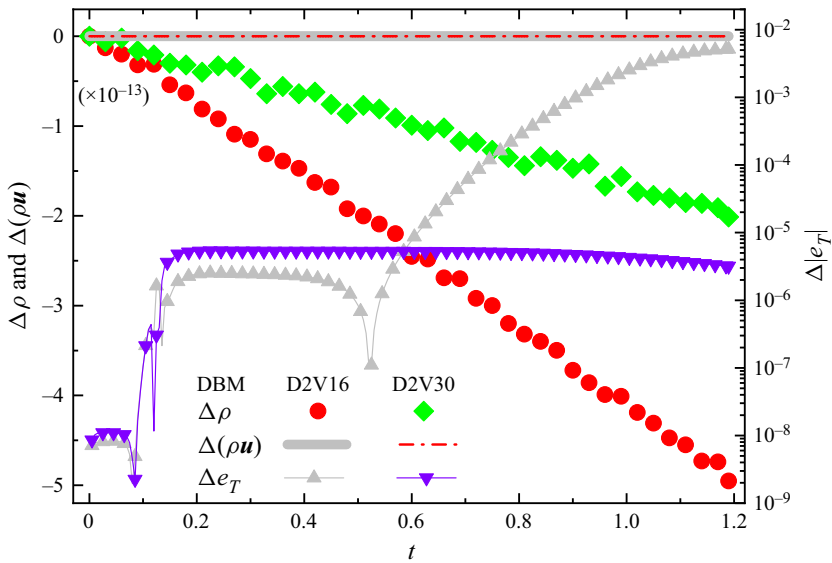


Figure 5. Variations in ρ , ρu and e_T in a thermal phase separation process obtained from D2V16 and D2V30 DBMs.

that the retrieval of higher-order kinetic moments in physical modelling makes the DBM more powerful in inhibiting spurious currents.

3.1.3. Conservativeness of the new model

To examine the conservativeness of the new model, we monitor variations in ρ , ρu and e_T in a thermal phase transition process in figure 5. The initial conditions are $(\rho, T, u_x, u_y) = (1.5 + \Delta, 1.0, 0.0, 0.0)$, where Δ is a random noise of the amplitude 0.001 acting as heterogeneous nuclei and accelerating the kinetic process. The remaining parameters are $N_x = N_y = 128$, $\tau = 10^{-3}$, $K = 5 \times 10^{-5}$ and $\text{Pr} = 0.1$. Even when the system is quenched instantaneously to a completely unstable state, the two models maintain $\Delta\rho$ and $\Delta(\rho u)$ to machine accuracy. Meanwhile, it is found that $\delta(\rho u)$ is two orders of magnitude lower than $\delta(\rho)$. This is because: (a) $\delta(\rho u) = u \delta\rho + \rho \delta u$; (b) different from the isothermal phase separation process, the release of latent heat causes the changing of local temperature. The freedom in temperature results in a more detailed and stricter local mechanical and thermodynamic equilibrium, consequently hampering the full development of velocity, especially for the case with large viscosity. The mean velocity u_{mean} is approximately of the order of 10^{-2} throughout the simulations that we considered. So $u\delta\rho \sim 10^{-15}$. (c) Furthermore, it is reasonable that variations in $\rho(t)$ and $\rho u(t)$ are proportional to their fluctuations, $\delta\rho \propto (\rho_{max} - \rho_{min}) \sim o(1)$ and $\delta u \propto (u_{max} - u_{min}) \sim o(10^{-2})$, so δu is two orders of magnitude lower than $\delta\rho$. Then $\rho \delta u \sim 10^{-15}$.

In our simulations, the average energy density $e_T = \rho T - a\rho^2 + K|\nabla\rho|^2/2 + \rho u^2/2 = -3.000015$. Different from $\Delta\rho$ and $\Delta(\rho u)$, $\Delta e_T(t)$ oscillates and grows persistently during the whole procedure mimicked by the D2V16 model. Two reasons account for the oscillation and growth in $\Delta e_T(t)$. First, the appearance of numerous liquid–vapour interfaces in the spinodal decomposition stage induces macroscopic quantity gradients and accumulated spatial discretization errors. Second, the resulting macroscopic quantity gradients serve as sources of HNE and TNE that may threaten the validity of the

lower-order DBM. The maximum deviation of $e_T(t)$ is 0.01 for the D2V16 model, while it is $O(10^{-6})$ for the D2V30 model, demonstrating that the D2V30 model is more effective in maintaining energy conservation and more capable of handling typical non-equilibrium processes. These variations are indicators of model accuracy that significantly affect the phase morphology, flow field distribution and stability of simulation.

The results for two-dimensional lattices with 13, 15, 16 and 30 velocities indicate that increasing the order of approximation of the lattice Boltzmann equation enhances performance in maintaining thermodynamic consistency, energy conservation, and inhibiting spurious currents.

3.2. Multi-scale model and trans-scale ability

In the DBM modelling, there exist two sets of macroscopic variables, the conservative set $(\rho, \rho \mathbf{u}, e_T)$ and the non-conservative counterpart $(\Delta_{m,n}$ and $\Delta_{m,n}^*$, $m - n \geq 2$), which vary in diverse time and length scales. Compared with the slowly varying conservative variables, the THNE quantities are quickly varying non-conservative ones, with extremely short relaxation times of the order of 10^{-10} s (Myong 1999). In this subsection, we evaluate carefully the multi-scale predictive capability of the DBMs for describing THNE features. Specifically, we determine whether or not the DBM can correctly capture the fast-changing THNE characteristics around an evolving liquid–vapour interface. Indeed, understanding precisely the fine structure and the specific status of non-equilibrium state between two phases at coexistence is of central importance in a variety of fields, because these non-equilibrium characteristics determine the transport efficiency of mass and energy across an interface, as well as the growth dynamics and morphological behaviours.

To date, significant progress has been made by pioneers in the non-equilibrium effects of multiphase flows. Frezzotti *et al.* comprehensively studied the rich array of non-equilibrium effects of multiphase flows through solving numerically the Enskog–Vlasov equation by direct simulation Monte Carlo (Enskog–Vlasov DSMC) and through the molecular dynamics (MD) method (Frezzotti, Gibelli & Lorenzani 2005; Frezzotti 2011; Frezzotti & Rossi 2012; Frezzotti *et al.* 2018; Frezzotti, Barbante & Gibelli 2019), including the non-equilibrium structure of the liquid–vapour interface, velocity slip at the liquid–vapour boundary, non-equilibrium evaporation, and non-equilibrium stress. In addition to microscopic MD and mesoscopic DSMC, recently, the extended macroscopic moment method, in particular the regularized moment method (Struchtrup & Torrilhon 2003; Struchtrup 2005; Chen *et al.* 2016; Torrilhon 2016), derived as approximations of the Boltzmann equation by means of the order-of-magnitude method, has been developed rapidly and extended to the field of multiphase flows (Struchtrup *et al.* 2017; Struchtrup & Frezzotti 2022) by Struchtrup *et al.* In Struchtrup *et al.* (2017), the macroscopic evaporation boundary conditions for regularized 13 (R13) moment equations have been derived from microscopic interface conditions of the Boltzmann equation, which extends the application range of the R13 equation to multiphase flows in the transition regime. More recently, in Struchtrup & Frezzotti (2022), a set of 26 moment equations for the Enskog–Vlasov equation has been derived by using the Grad moment method, which provides a computationally efficient and functionally unified approach for ideal and non-ideal fluid flows far from equilibrium. Besides, the coupled constitutive relations theory was developed to capture the remarkable rarefaction effects at small scales in the liquid–vapour phase transition processes (Rana *et al.* 2021). Meanwhile, the rarefaction effects in a head-on collision of two identical droplets are investigated via various lattice Boltzmann models with different degrees of precision

(Chen *et al.* 2022*b*). It is found that the rarefaction effects enhance the conversion from free energy to kinetic energy, and accelerate droplet coalescence. Parsa *et al.* presented an original and fundamental molecular dynamics lattice gas (MDLG) approach connecting lattice Boltzmann methods to physical reality (Parsa & Wagner 2017, 2020; Czelusniak *et al.* 2020; Pachalieva & Wagner 2021; Parsa, Kim & Wagner 2021). The key implementation of MDLG is an embedded coarse-graining procedure, i.e. mapping an MD simulation onto a lattice Boltzmann framework. It permits us to study any system that can be simulated with MD, including the non-ideal system with significant non-equilibrium fluctuations (Parsa & Wagner 2020), since the collision operator is informed by an underlying MD simulation. This approach can be considered as an optimal LBM or a more realistic coarse-grained fluctuating method. We stress that these microscopic (MD), mesoscopic (DSMC, LBM and DBM proposed here) and macroscopic (high-order moment method, extended hydrodynamics or generalized hydrodynamics models) models/methods, with different starting points and different emphases, have their own strengths and insights, and complement each other, but cannot replace each other. In addition, the developments of these methods have stages.

Although extensive experimental and theoretical studies have been designed and developed in the past decades to address this issue (Weeks 1977; Evans 1979; Bedeaux 1986; Onuki 2002; Aarts, Schmidt & Lekkerkerker 2004; Lang & Leiderer 2006; Bu, Kim & Vaknin 2014; Jaensson & Vermant 2018), the early stage of the liquid–vapour transition, i.e. the spinodal decomposition stage, where non-equilibrium effects are much more pronounced than the latter domain growth stage, still needs further investigations from the viewpoint of non-equilibrium thermodynamics. Early studies tend to focus on conserved quantities and slow variables, because these characteristics are relatively stable and easy to grasp (Osborn *et al.* 1995; Gonnella *et al.* 1997, 2007, 2010; Succi 2001; Xu *et al.* 2003; Sofonea *et al.* 2004; Onuki 2007, 2002; Gan *et al.* 2011, 2012*b*; Coclite *et al.* 2014). The study of these conserved quantities and slow variables provides a basis for the study of fast-changing behaviour that is particularly relevant to the early stage of spinodal decomposition, a process still far from being completely understood.

The reason is that these fast-varying and complex THNE quantities springing up in the spinodal decomposition stage are difficult to measure and analyse. Moreover, related experiments are costly and time-consuming. Theoretical analysis is usually limited to cases with numerous simplifying assumptions and generalizations, such as the local equilibrium assumption, given small deviations from the equilibrium state and linear relationship between fluxes and forces. How to overcome these limitations is a core problem in physical modelling (Gurtin & Voorhees 1996; Vilar & Rubi 2001; Schweizer, Öttinger & Savin 2016; Rana *et al.* 2021).

The definition of any non-equilibrium strength depends on the perspective of the study. Complex systems need to be investigated from multiple perspectives. If we look at the system from N angles, then there are N kinds of non-equilibrium strengths. Therefore, if the N kinds of non-equilibrium strengths are taken as components to introduce a non-equilibrium strength vector, then it should be more accurate and specific. Below, we use the four-component vector $\mathcal{S}_{THNE} = (\Delta_2, \Delta_{3,1}, \Delta_3, \Delta_{4,2})$, whose analytical expressions have been derived, to describe roughly the strength of non-equilibrium.

3.2.1. Weak THNE case

According to the analytical formulas listed in Appendix B and § 2.1, four explicit factors control the intensities and structures of THNE manifestations, i.e. the relaxation time τ , the fluid velocity \mathbf{u} , the gradient force, and the interparticle force caused by gradients

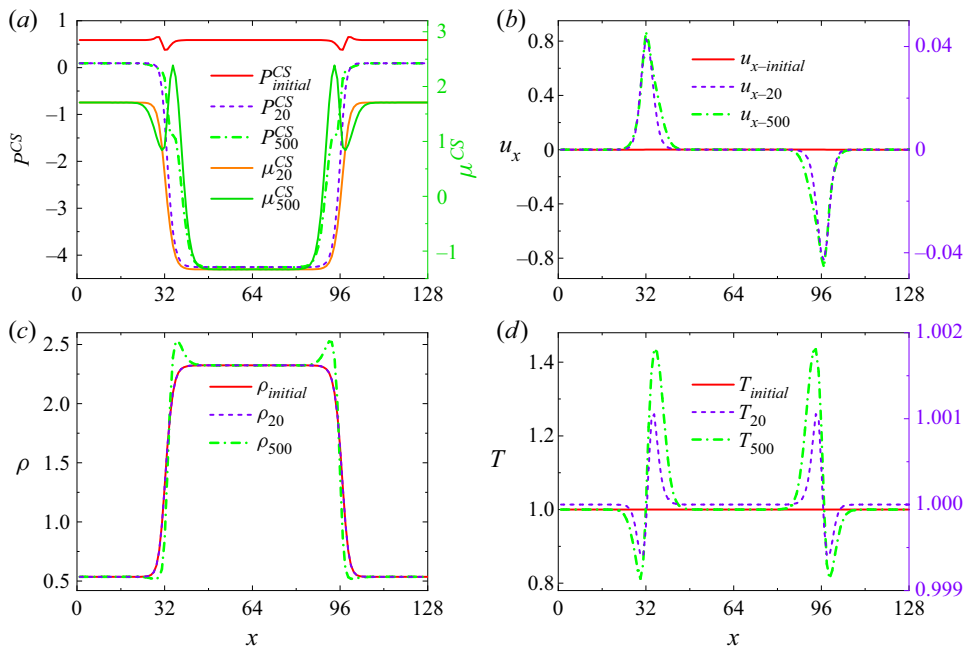


Figure 6. Profiles of hydrodynamic quantities calculated from the D2V30 model at three representative instants: 0, 20 and 500 iterations.

of macroscopic quantities. The latter are affected implicitly by the initial state and the duration of evolution, for example, the initial density distribution, the quenching temperature, the surface tension coefficient, and the Prandtl number. Therefore, by adjusting these aspects, we can design scenarios with weak, moderate and strong THNE strengths.

First, we investigate the weak THNE case. The initial state is the equilibrium density profile $\rho_{initial}(x)$ at $T = 1.74$, as shown in figure 6(c). The parameters are $K = 2.7 \times 10^{-5}$, $\Delta t = 2 \times 10^{-5}$ and $\Delta x = \Delta y = 5 \times 10^{-3}$; others are consistent with those in figure 3. When simulation starts, the system is suddenly quenched to $T = 1.0$. The profiles of hydrodynamic quantities, including the chemical potential (Wagner 2006; Wen *et al.* 2017, 2020) $\mu^{CS} = RT[(3 - b\rho/4)/(1 - b\rho/4)^3 + \ln \rho + 1] - 2a\rho - K \nabla^2 \rho$, calculated from the D2V30 model at representative instants, are shown in figure 6, where ϕ_n represents the macroscopic quantity after n iterations. The following results have been obtained. (i) The instantaneous decrease in temperature results in the emergence of steep gradients in both pressure P^{CS} and chemical potential μ^{CS} near the liquid–vapour interfaces (see figure 6a). (ii) The pressure and chemical potential gradients drive the vapour phase across the interface towards the liquid phase (see figures 6b,c), contributing to the decrease (increase) in vapour (liquid) density, and the appearance of remarkable velocity around the interface. After 20 iterations, the maximum velocity along the x direction, u_{x-max} , is approximately 0.04, but it exceeds 0.80 after 500 iterations. (iii) With the development of phase separation, latent heat is released locally to and absorbed by the surrounding liquid and vapour phases, respectively. These processes lead to violent changes in temperature and local mechanical imbalance. The maximum temperature difference between the two phases ΔT_{max} is negligible at the very beginning of the procedure, but reaches $0.6T_{initial}$ at

$t = 0.01$ (500 iterations), which is the largest difference from an isothermal case at a fixed temperature.

Figure 7 portrays the specific THNE manifestations Δ_{2xx} , $\Delta_{3,1x}$, Δ_{3xxx} , and $\Delta_{4,2xx}$ for figure 6 at $t = 4 \times 10^{-4}$ (20 iterations), where the D2V13 model at the NS level (left column), the D2V15 model at the NS level (middle column), and the D2V30 model beyond the third-order super-Burnett level (right column) have been adopted. For the convenience of comparisons, analytical solutions with the first- and second-order accuracies are plotted by solid lines. Figure 7 shows the following general characteristics when the system deviates from thermo-hydrodynamic equilibrium. (i) THNE effects concentrate primarily in the interfacial regions, where the interparticle force and gradient force dominate, and disappear in the same manner as the gradients of macroscopic quantities vanish in the liquid and vapour bulk phases. (ii) Owing to the limited action time of the gradient force and interparticle force, THNE effects are not fully developed until this moment. (iii) The first-order THNE, $\Delta_{m,n}^{(1)} \propto \tau$, is always larger than the second-order THNE, $\Delta_{m,n}^{(2)} \propto \tau^2$, demonstrating that $\Delta_{m,n}^{(1)}$ is the principal part of $\Delta_{m,n}$ and, to some extent, the effectiveness of the lower-order coarse-grained model. (iv) It is interesting to find that $|\Delta_{m,n}^{(1)} + \Delta_{m,n}^{(2)}|$ is not larger than $|\Delta_{m,n}^{(1)}|$, i.e. the second-order THNE invariably acts as negative feedback on the first-order one, and weakens the total THNE intensity.

Beyond the aforementioned commonalities, the following distinctive performances among various models should be examined thoroughly. It is clear that even with such a feeble THNE, the simulation results of the D2V13 and D2V15 models do not match well, with either the first-order or the second-order theoretical solutions. More explicitly, the two lower-order models overestimate the THNE level tremendously, especially on the vapour side and for the xxx component of Δ_3 . The discrepancies possess peak values approximately at the locations where the gradient of the most associated physical quantity reaches its local maximum (minimum).

Two key factors are responsible for the failure of the lower-order DBM in capturing THNE accurately. On the one hand, to fully describe a given non-equilibrium quantity $\Delta_{m,n}^{(j)}$, the number of the required kinetic moments retrieved exactly by the discrete equilibrium distribution function $f_i^{(0)}$ increases with increasing m , i.e. the rank of $\Delta_{m,n}$. As shown in table 1, in the formulation of $\Delta_{3,1}^{(1)}$, $f_i^{(0)}$ should satisfy the moment $M_{5,1}$; when deriving $\Delta_{4,2}^{(1)}$, $f_i^{(0)}$ should satisfy higher-order moments $M_{5,3}$ and $M_{6,2}$. On the other hand, additional moment constraints on $f_i^{(0)}$ need to be selected and guaranteed with increasing j , i.e. the order of accuracy of $\Delta_{m,n}$. Concretely, a first-order accuracy in the description of Δ_3 can be achieved by maintaining M_4 and M_5 ; while realizing a second-order accuracy in the description of Δ_3 , $f_i^{(0)}$ should further retain the additional thermodynamic one, $M_{6,4}$ ($M_{5,3}$ in table 1 is not independent of M_5). Table 2 manifests that both the D2V13 and D2V15 models cannot hold these necessary constraint relationships, even just for the first-order accurate descriptions of $\Delta_{3,1}^{(1)}$ and $\Delta_{4,2}^{(1)}$. Among these THNE quantities, the correct description of Δ_3 and $\Delta_{4,2}$ requires the retrieval of the highest-order moment relations. Thus, as expected, the worst simulation results appear in figures 7(c.i), (c.ii), (d.i) and (d.ii), provided by the two lower-order models.

Compared with the D2V13 model, the supplemental moment $M_{5,1}$, which is necessary for the formulation of $\Delta_{3,1}^{(1)}$ and maintained by the D2V15 model, plays a fairly negligible role in improving the numerical precision of $\Delta_{3,1x}$, because the second-order

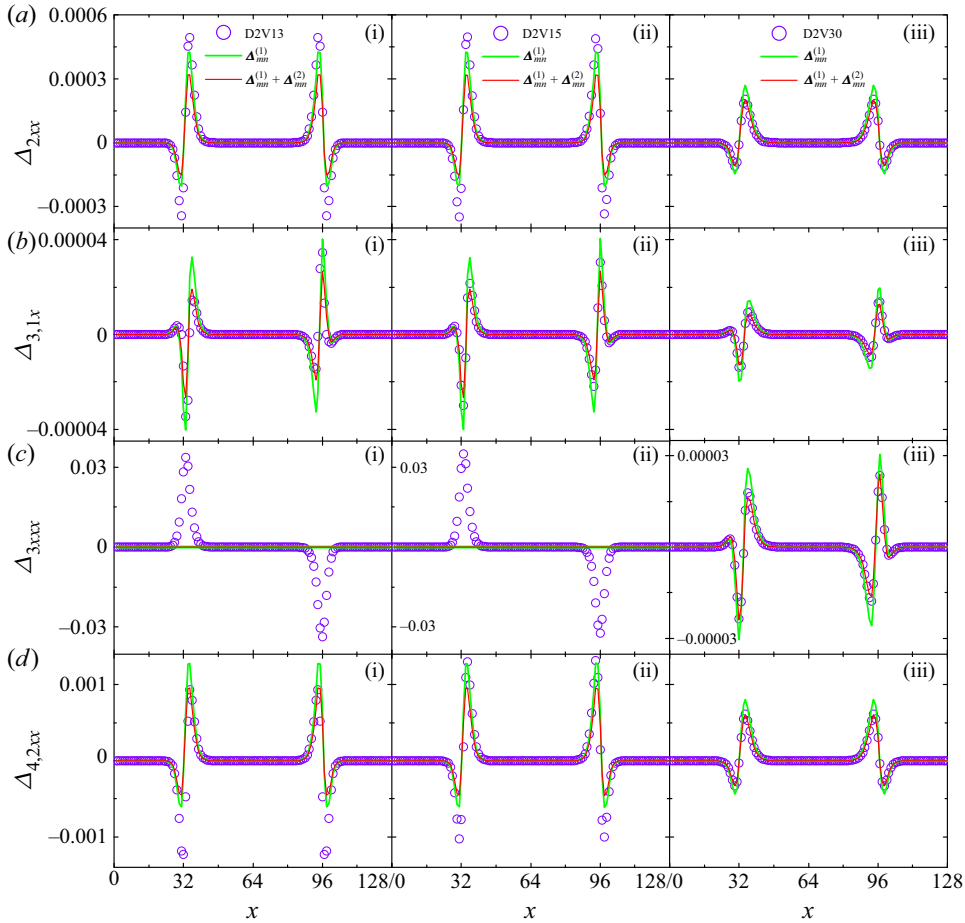


Figure 7. Weak case: THNE manifestations calculated from DBMs at various levels and theoretical analysis. Here, $t = 4 \times 10^{-4}$ (20 iterations) and $\tau = 10^{-4}$.

non-equilibrium effects $\Delta_{m,n}^{(2)}$ cannot be neglected in contrast to the first-order $\Delta_{m,n}^{(1)}$ during the early stage of spinodal decomposition. Under this condition, considering the first-order THNE effects only is not recommended. Indeed, at the beginning of the phase separation, the gradients of temperature and velocity approximately equal zero. As a result, $\Delta_{2xx}^{(1)} \simeq 0$, and $\Delta_{2xx}^{(2)}$ can be simplified to $(T^2/\rho)(\partial_x \rho)^2 - T^2(\partial^2 \rho/\partial x^2) - \rho T^2 \partial_x B_x$. These higher-order terms in $\Delta_{2xx}^{(2)}$ do not appear in classical hydrodynamics, but are essential for modelling a system far from equilibrium (Struchtrup 2005; Struchtrup & Frezzotti 2022). Other non-equilibrium measures can be analysed similarly. That is, interparticle force and density gradient force first trigger the second-order THNE, and afterwards, stimulate the first-order THNE through enlarging velocity and temperature gradients. To evaluate under which circumstances the higher-order THNE should be taken into account, a characteristic dimensionless parameter, called the relative THNE strength $R_{THNE} = |\Delta_{m,n}^{(j+1)} / \Delta_{m,n}^{(j)}|$, may be introduced for the estimation of the relative importance of the $(j + 1)$ th-order THNE effects to the j th-order ones. The R_{THNE} for Δ_{2xx} , $\Delta_{3,1x}$, Δ_{3xxx} and $\Delta_{4,2xx}$ at the positions where these non-equilibrium measures take extreme values, are 0.250, 0.349, 0.212 and

0.252, respectively. At earlier times, such as after 15 iterations, R_{THNE} is as high as 0.50. Therefore, higher-order DBMs with at least second-order accuracy for $\Delta_{m,n}$ are undoubtedly needed, even for cases with faint non-equilibrium effects. Tables 1 and 2 indicate that the D2V30 model satisfies all the needed kinetic moment relations. Consequently, the D2V30 results are consistent with the theoretical analysis at the second order of accuracy. In particular, the remarkable deviations in figures 7(c.i) and (c.ii) disappear in figure 7(c.iii).

3.2.2. Moderate THNE case

As time evolves, the degree of phase separation becomes pronounced, with extended phase-separating regions and prominent gradients of macroscopic quantities (see dash-dot lines in figure 6). The non-equilibrium manifestations at the same instant, exhibited in figure 8, indicate that the system enters into the moderate THNE stage. Compared with figure 7, the most distinctive difference in figure 8 is the enormous growth in $\Delta_{m,n}$, approximately 10–1000 times larger than in the weak case. For each kind of THNE quantity, the first-order analytical solution (denoted by green dots) overlaps with the second-order one (denoted by red solid lines), illustrating that $\Delta_{m,n}^{(2)}$ is negligible compared with $\Delta_{m,n}^{(1)}$. Correspondingly, the relative THNE strengths R_{THNE} for Δ_{2xx} , $\Delta_{3,1x}$, Δ_{3xxx} and $\Delta_{4,2xx}$ are as small as 0.006, 0.002, 0.018 and 0.016, respectively. For Δ_{2xx} , good agreements between simulations and theoretical solutions are depicted in figures 8(a.i) and (a.ii). This is understandable because either of the D2V13 and D2V15 models is a sufficient description of $\Delta_{2xx}^{(1)}$. Nevertheless, for $\Delta_{3,1x}$, owing to the lack of indispensable kinetic moment $M_{5,1}$ in the D2V13 model, distinct discrepancies are found in figure 8(b.i), but are absent in figure 8(b.ii), obtained from the D2V15 model that meets the constraint of $M_{5,1}$. Similarly, for Δ_{3xxx} and $\Delta_{4,2xx}$, the D2V13 and D2V15 results mismatch the theoretical profiles, because of the deficiencies in the necessary high-order moments M_4 , M_5 and $M_{6,2}$. By contrast, as shown in the third column of figure 8, the D2V30 results coincide excellently with the theoretical results, regardless of the relative non-equilibrium intensity. We also stress that if we focus only on the hydrodynamic quantities and constitutive relations (related to Δ_2 and $\Delta_{3,1}$), but not the evolution of the constitutive relations (related to Δ_3 and $\Delta_{4,2}$), then the D2V15 model is reliable and acceptable when R_{THNE} is small enough.

3.2.3. Strong THNE case

To further examine the multi-scale ability of the models, we increase the strength of THNE measures by straightforwardly increasing the relaxation time τ in figure 9. In addition, another way to control the THNE strength is by adjusting the quenching depth T/T_C , which indirectly affects the non-equilibrium intensity by changing the gradients of hydrodynamic quantities. With the increasing of THNE intensity, deviations between lower-order DBM simulations and theoretical solutions become extraordinarily conspicuous (see the first and second columns of figure 9). The relative THNE strengths R_{THNE} for Δ_{2xx} , $\Delta_{3,1x}$, Δ_{3xxx} and $\Delta_{4,2yy}$ rapidly reach up to 0.213, 0.248, 0.169 and 0.239, respectively, manifesting the importance of the second-order THNE and the urgent need for a higher-order DBM. The D2V30 model meets the minimum physical requirements in describing accurately the concerned THNE quantities. Therefore, the reasonable agreements between D2V30 simulations and corresponding theoretical solutions in the weak, moderate and strong THNE cases demonstrate comprehensively that the D2V30

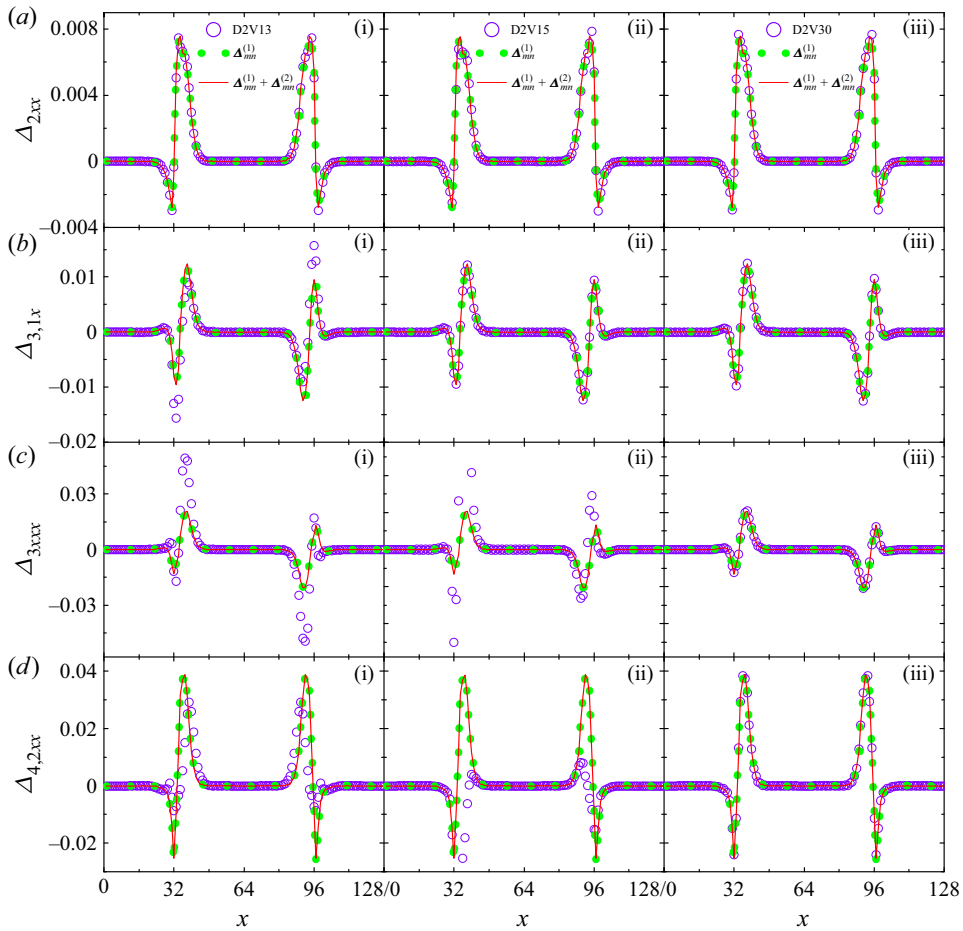


Figure 8. Moderate case: non-equilibrium manifestations calculated from DBMs at various levels and theoretical analysis. Here, $t = 0.01$ (500 iterations) and $\tau = 10^{-4}$.

DBM is indeed a multi-scale model and possesses better trans-scale ability than the D2V13 and D2V15 models.

To assess the application range of the DBM more completely, we resort to the Knudsen number, a dimensionless parameter generally used to characterize non-equilibrium or rarefaction degree of flows, and classify various flow regimes. The Knudsen number $Kn = \lambda/L$ is defined as the ratio of the mean free path $\lambda = c_s \tau$ to a characteristic length that we focus on, $L = \Theta/|\nabla\Theta|$, where c_s is the local speed of sound, and Θ is a physical quantity. The maximum Kn_{max} values calculated by density for cases with weak, moderate and strong THNE effects are 0.008, 0.015 and 0.141, respectively, all beyond the application scope of NS equations. Evidently, the applicable range of the D2V30 model has been extended into the early transition regime.

3.3. Effects of relaxation time on TNE

In this subsection, we investigate the multi-scale limit of the D2V30 model through exploring whether the model can correctly reproduce higher-order constitutive relations for multiphase flows over a wide range of relaxation times and Knudsen numbers.

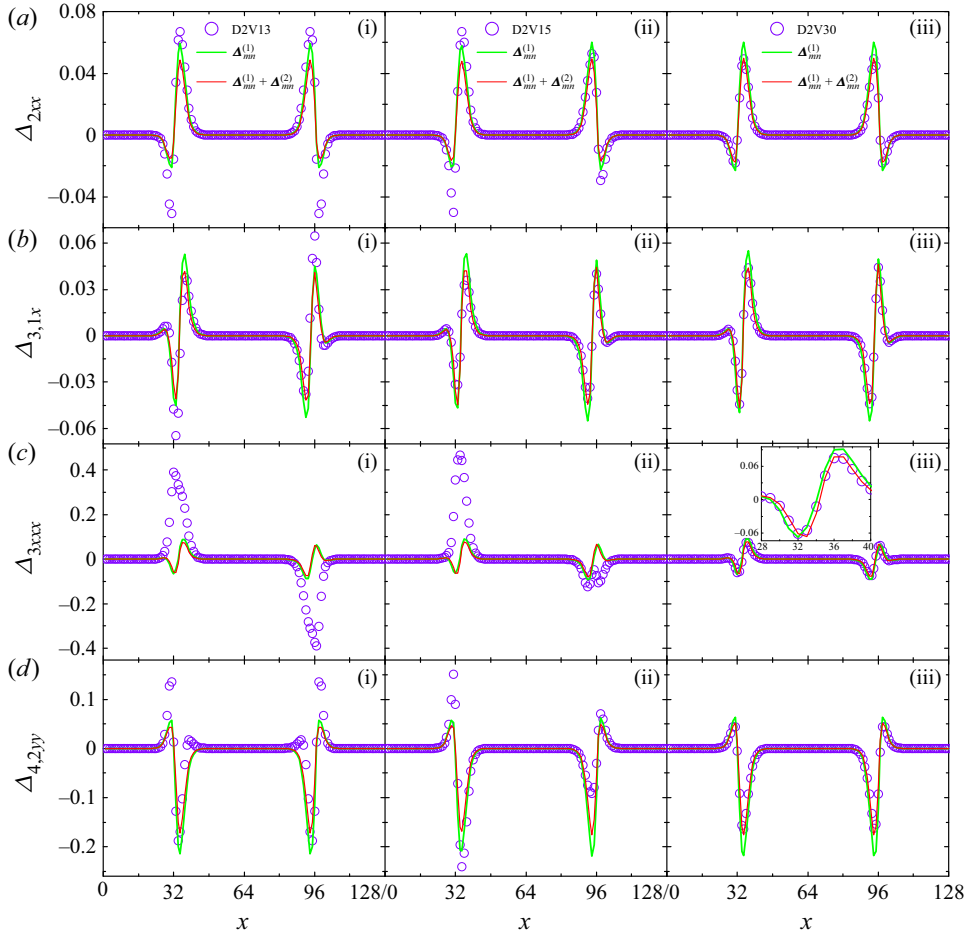


Figure 9. Strong case: non-equilibrium manifestations calculated from DBMs at various levels and theoretical analysis. Here, $t = 0.006$ (300 iterations) and $\tau = 10^{-3}$.

Essentially, the accurate description of constitutive relations is of fundamental importance to the simulation of highly non-equilibrium multiphase flows (Struchtrup 2005). It is the constitutive relations that determine directly the multi-scale ability and accuracy of a model. For this purpose, in figure 10, we exhibit the effects of relaxation time τ on the two typical TNE manifestations: viscous stress (left column) and heat flux (right column) at $t = 0.01$, where the initial conditions and parameters in figure 7 are used, except for $K = 5 \times 10^{-5}$. To be seen is that the magnitudes of $\Delta_{2,xx}^*$ and $\Delta_{3,1x}^*$, and the discrepancies between DBM simulations and the second-order theoretical solutions, increase as τ increases. Specifically, for the case with $\tau = 3 \times 10^{-3}$, excellent coincidences can be observed between the two counterparts. When τ increases to 4×10^{-3} , good agreements can be found, whereas when τ further increases to 5×10^{-3} , noticeable oscillations and distinctions, labelled by green rectangles, emerge around the interfaces in figures 10(c.i) and (c.ii), respectively.

Apart from the relative TNE intensity $R_{TNE} = |\Delta_{m,n}^{*(j+1)} / \Delta_{m,n}^{*(j)}|$, the aforementioned TNE discrepancy between DBM simulation and theoretical solution, $\mathcal{R}_{Dis} = \Delta_{DBM}^* - \Delta_{Exact}^*$, or the relative TNE discrepancy $R_{Dis} = |(\Delta_{DBM}^* - \Delta_{Exact}^*) / \Delta_{Exact}^*|$ can be regarded as

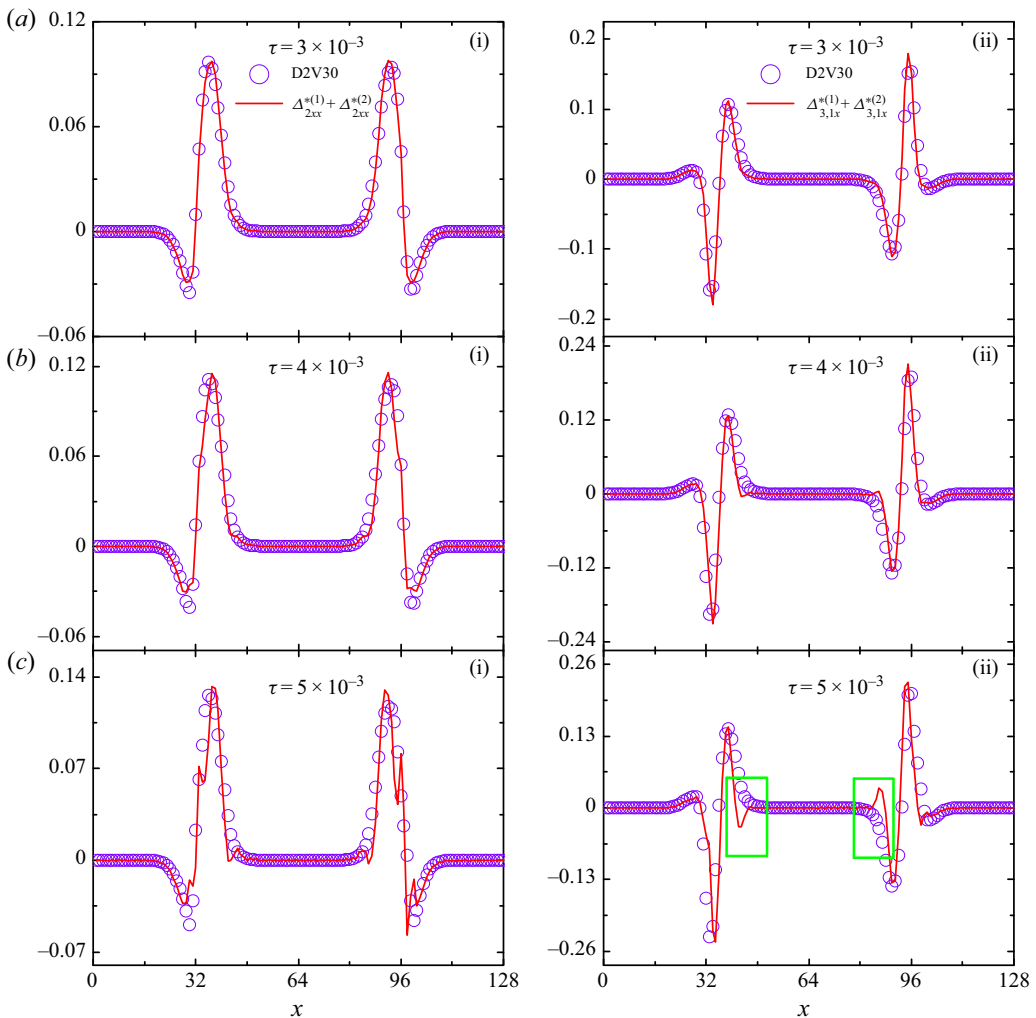


Figure 10. Effects of relaxation time on typical TNE manifestations: viscous stress (left column) and heat flux (right column).

a non-equilibrium criterion for assessing the effectiveness of a coarse-grained model and appropriateness of the coarse-graining process, as shown in § 2. In real simulations, only when R_{TNE} or R_{Dis} is negligibly small is the proposed DBM physically sufficient and appropriate. Otherwise, a higher-order DBM that considers higher-order TNE effects should be adopted. Thus from this point of view, the critical relaxation time for the D2V30 model is $\tau_C = 4 \times 10^{-3}$ with respect to this standard test. When $\tau > \tau_C$, the present model is ineffective and unacceptable, and contributions of high-order departures from equilibrium distribution function $f^{(j)}$ ($j > 2$) should be considered in physical modelling.

Figure 11 further demonstrates that higher-order constitutive relations are necessary for obtaining accurate hydrodynamic quantities and fine structures of material and mechanical interfaces as the degree of non-equilibrium deepens ($\tau = 4 \times 10^{-3}$), where $\varphi_M - \varphi_N$ represents the hydrodynamic quantity difference calculated from models with M and N discrete velocities. The maximum relative error in the velocity profile is 28.4% at this

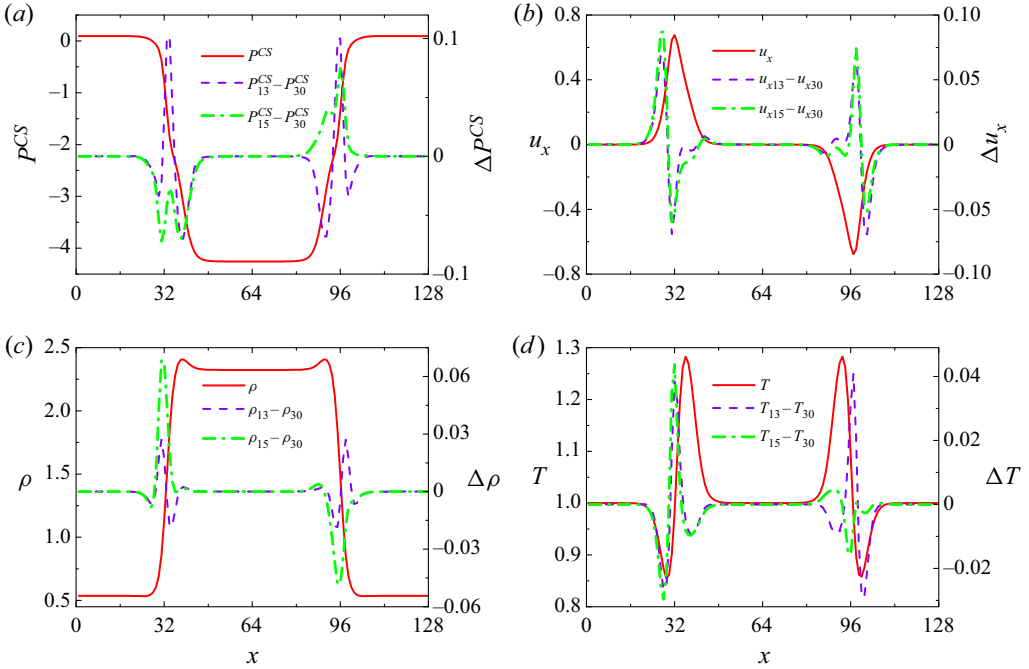


Figure 11. Hydrodynamic quantities calculated from the D2V30 model, and the corresponding differences among the D2V30, D2V15 and D2V13 models at $t = 0.01$ when $\tau = 4 \times 10^{-3}$.

moment, typically located at the highly non-equilibrium regime, but quickly reaches up to 70.0 % after 200 iterations with the accumulation of errors. This kind of error, belonging to the physical modelling aspect, cannot be reduced or eliminated by improving the accuracy of the algorithm. The inaccuracy of the D2V13 and D2V15 models is due to the crucial missing of some necessary higher-order moments required for recovering $f^{(j)}$ ($j \geq 2$).

Subsequently, we illustrate the effects of relaxation time on the slowly and quickly varying variables in figure 12. Figures 12(a,b) demonstrate how relaxation time τ affects the maximum viscous stress $\Delta_{2xx-max}^*$ and the maximum heat flux $\Delta_{3,1x-max}^*$. Clearly, τ strengthens the intensities of $\Delta_{2xx-max}^*$ and $\Delta_{3,1x-max}^*$ in the same manner. The relationship between $\Delta_{2xx-max}^*$ ($\Delta_{3,1x-max}^*$) and τ can be divided into two stages: linear and nonlinear. When $\tau \leq \tau_0$, $\Delta_{2xx-max}^*$ ($\Delta_{3,1x-max}^*$) increases linearly with τ , $\Delta_{2xx-max}^* = B_2\tau$ ($\Delta_{3,1x-max}^* = B_4\tau$); when $\tau > \tau_0$, the linearization is no longer valid, and the dependence of $\Delta_{2xx-max}^*$ ($\Delta_{3,1x-max}^*$) on τ can be fitted by $\Delta_{2xx-max}^* = A_1 + B_1\tau^{2/3}$ ($\Delta_{3,1x-max}^* = A_3 + B_3\tau^{2/3}$), manifesting the necessity of higher-order constitutive relations for a system far away from equilibrium. The fitting parameters are $A_1 = -0.006$, $B_1 = 4.889$, $B_2 = 45.000$, $A_3 = -0.014$, $B_3 = 8.231$ and $B_4 = 69.291$. Of course, the ending point of the linear constitutive relations provides a distinct criterion to identify whether the system is near or far from equilibrium. Figure 12(c) shows distributions of the local Knudsen number $Kn(x)$ with various τ . Similar to the behaviours of THNE, $Kn(x)$ becomes more pronounced in the interfacial region, and reaches its maximum at the point at which the gradient of quantity attains its peak value; it vanishes exponentially in the bulk of the liquid and vapour regions. The maximum interface Knudsen number Kn_{max} calculated from density exceeds $1/3$, indicating that the D2V30 model is valid in the transition flow regime.

DB multi-scale modelling of non-equilibrium multiphase flows

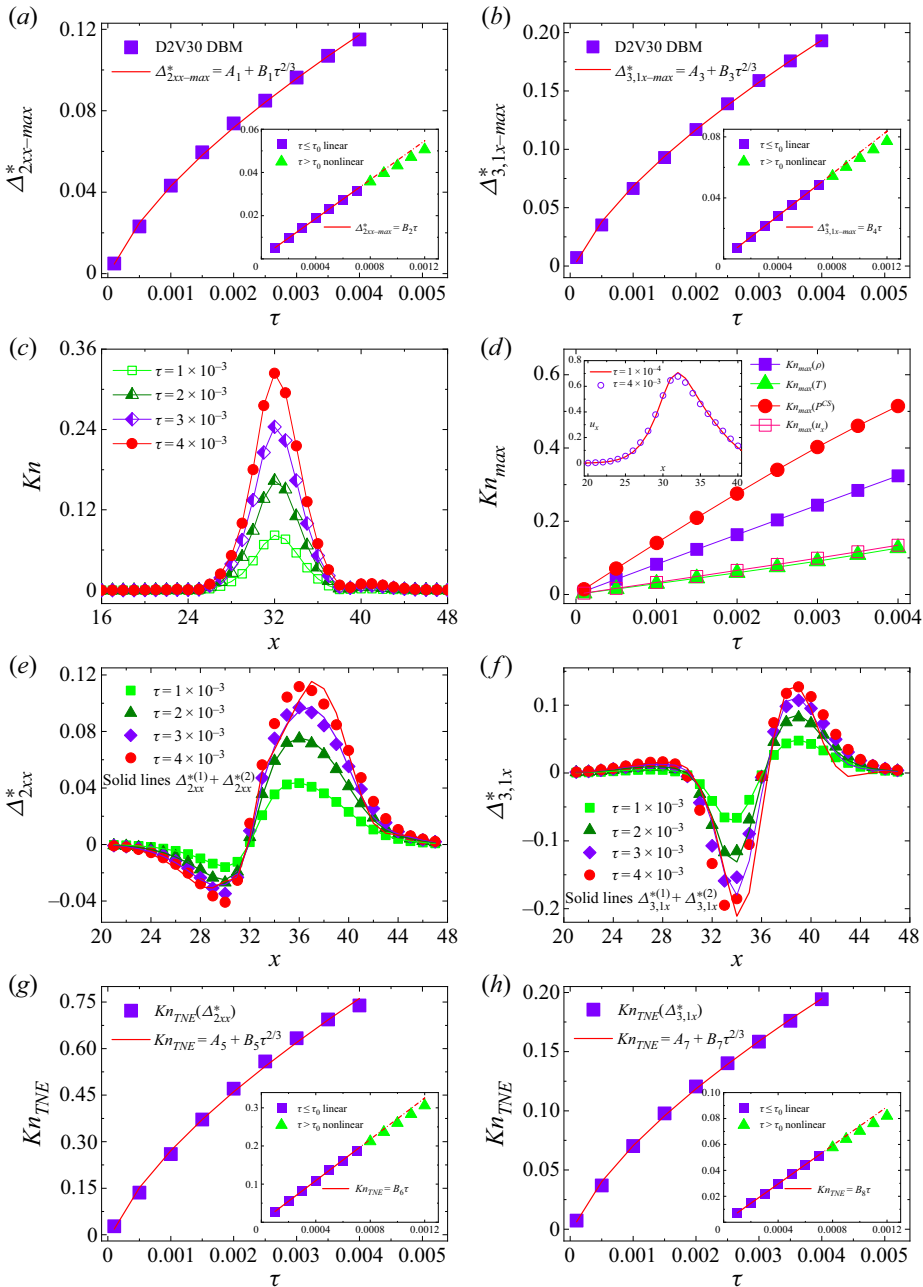


Figure 12. Effects of relaxation time on the maximum viscous stress (a), the maximum heat flux (b), distributions of the local Knudsen number (c), the maximum Knudsen number (d), distributions of viscous stress (e), distributions of heat flux (f), the Knudsen number calculated from viscous stress (g), and the Knudsen number calculated from heat flux (h).

Different from the ideal gas system and the effects of surface tension, the relaxation time τ only enlarges the amplitude of Kn , but does not extend the non-equilibrium region, or broaden the characteristic length scale of a system, resulting in the approximately linear dependence of $Kn_{max}(\rho, T, P^{CS}, u_x)$ on τ , as shown in figure 12(d). This is because

the slowly varying variables appear to be slightly affected (for $u_x(x)$, see the legend of figure 12d) or basically unaffected (for $\rho(x)$, $T(x)$, $P^{CS}(x)$, not shown here) by relaxation time until this moment, but noteworthy smoothed by the surface tension coefficient (see figures 13c,d). From this perspective, the interface Knudsen number calculated from the slowly varying quantity cannot be viewed as a qualified parameter to characterize the non-equilibrium behaviours at the early stage of phase separation.

To solve this issue, we therefore resort to the quickly varying quantities, i.e. the TNE measures, and Knudsen numbers calculated from them. Figures 12(e) and 12(f) show effects of the relaxation time on viscous stresses and heat fluxes, where symbols represent DBM simulation results, and solid lines indicate the corresponding theoretical estimates. As shown in figures 12(e,f), the relaxation time substantially improves the magnitudes of TNE measures and changes their structures. The characteristic length scales are extraordinarily sensitive to relaxation time, position and time. Figures 12(g,h) suggest that the relaxation time significantly enhances the maximum Knudsen numbers calculated from viscous stress, $Kn_{max}(\Delta_{2xx}^*)$ (figure 12g), and heat flux, $Kn_{max}(\Delta_{3,1x}^*)$ (figure 12h). The $Kn_{TNE} \sim \tau$ relation behaves qualitatively similarly to the one between $\Delta_{2xx-max}^*$ ($\Delta_{3,1x-max}^*$) and τ . The moderate growth in Kn_{TNE} when $\tau > \tau_0$ results from the second-order TNE effect that restrains the total TNE intensity.

3.4. Effects of surface tension on TNE

Here, the focus is on how and to what extent surface tension affects the dynamic patterns and TNE features. Figures 13(a) and 13(b) show the viscous stresses and heat fluxes at $t = 0.01$ for cases with various surface tension coefficients K , where symbols stand for simulation results, and solid lines represent the corresponding second-order analytical solutions. The initial conditions and other parameters are the same as those in figure 9. As shown, the surface tension effects are threefold, restraining the local TNE intensity near the interface, but expanding the TNE range and strengthening the TNE intensity away from the interface (see the solid lines and the red arrows in legends for details), through interface smoothing and extending. This result can also be verified by figures 13(c,d), where the maximum of Kn decreases but the region with non-zero Kn increases with K , as a result of the capillary wave broadening. When K varies in the interval $[3 \times 10^{-5}, 18 \times 10^{-5}]$, the dependence of $Kn_{max}(\rho)$ and $Kn_{max}(T)$ on K can be fitted by $Kn_{max}(\rho) = A_9 + B_9/K$ and $Kn_{max}(T) = A_{10} + B_{10}/K$, respectively, with $A_9 = 0.013$, $B_9 = 3.422 \times 10^{-6}$, $A_{10} = -0.003$, and $B_{10} = 1.588 \times 10^{-6}$. The high sensitivity of density profile to surface tension coefficient (see the legend of figure 13d) is due mainly to the \mathbf{A} term in (2.2) that is linearly proportional to K .

Accordingly, as plotted in figures 13(e,f), the maxima of Δ_{2xx}^* and $\Delta_{3,1x}^*$ decrease synchronously with K approximately as $\Delta_{2xx-max}^* = A_{11} + B_{11}/K^{1/2}$ and $\Delta_{3,1-max}^* = A_{12} + B_{12}/K$, with $A_{11} = -0.023$, $B_{11} = 4.667 \times 10^{-4}$, $A_{12} = 0.008$ and $B_{12} = 3.711 \times 10^{-6}$. In other words, large resistances to mass and heat transfers appear at the interface, and increase with the surface tension coefficient. The suppressive effect of surface tension on heat flux is much stronger than that on viscous stress at a small Prandtl number. We further examine the effects of surface tension on TNE in terms of the capillary number Ca , which denotes the ratio between viscous force and interfacial tension, $Ca = \mu u_C / \sigma$, with u_C the characteristic velocity, and σ the interfacial tension between liquid and vapour phases. For a planar interface, σ can be computed specifically as $\sigma = K \int_{-\infty}^{\infty} (\partial \rho / \partial z)^2 dz$. Figures 13(g,h) show relations among TNE measures and the

DB multi-scale modelling of non-equilibrium multiphase flows

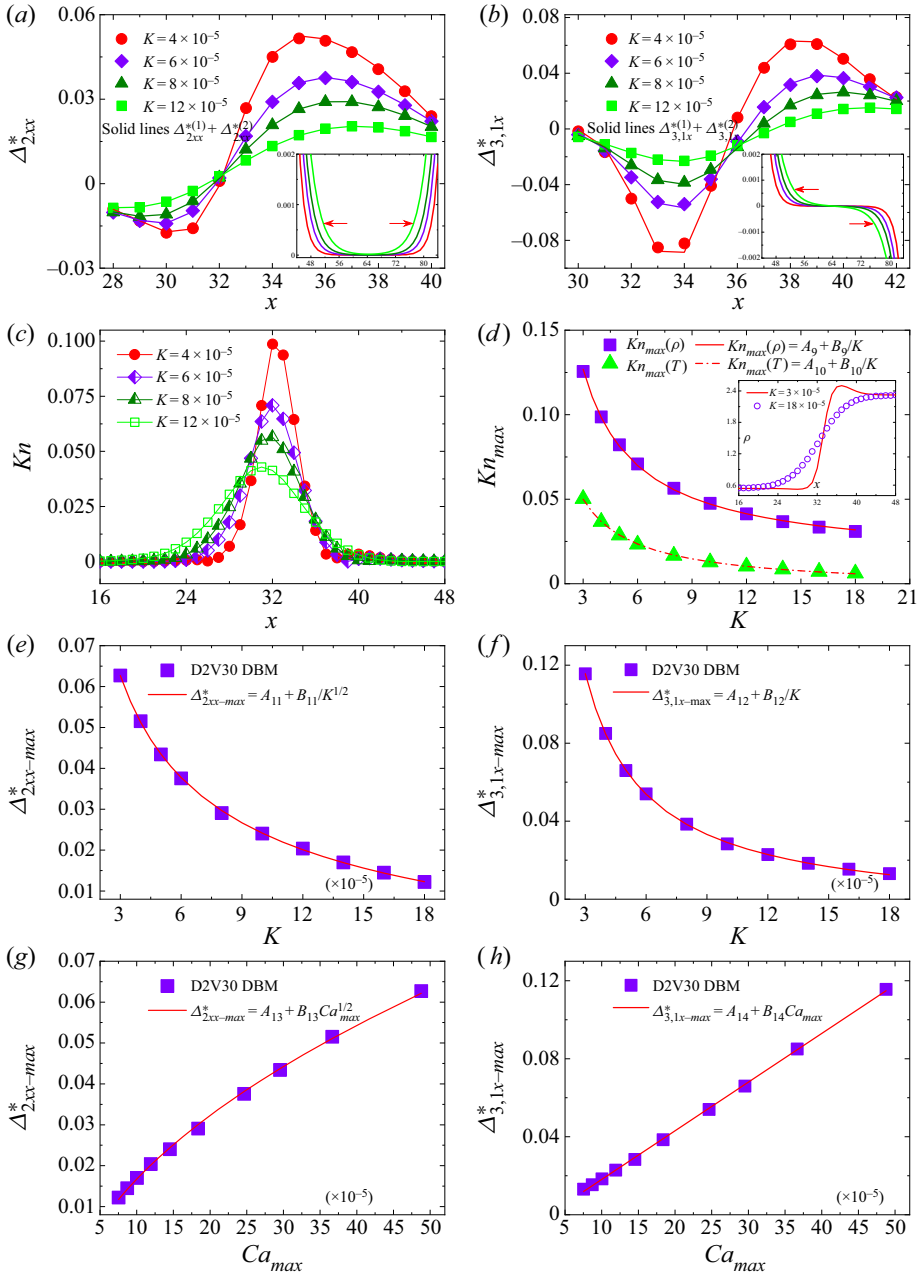


Figure 13. Effects of surface tension coefficient on the distributions of viscous stress (a), heat flux (b), the local Knudsen number (c), the maximum of Knudsen numbers calculated from density and temperature (d), the maximum viscous stress (e), and the maximum heat flux (f). Also, the relation between the maximum viscous stress and the maximum Capillary number (g), and the relation between the maximum heat flux and the maximum Capillary number (h).

maximum capillary number Ca_{max} . Clearly, Δ_{2xx}^* and $\Delta_{3,1x}^*$ increase with increasing Ca_{max} . The two relations can be fitted by $\Delta_{2xx}^* = A_{13} + B_{13} Ca_{max}^{1/2}$ and $\Delta_{3,1x}^* = A_{14} + B_{14} Ca_{max}$, with fitting parameters $A_{13} = -0.021$, $B_{13} = 3.761$, $A_{14} =$

-0.007 and $B_{14} = 249.513$. The diametrically opposite trends in figures 13(e) and 13(g) (also figures 13(f,h)) are due to the inverse relation between Ca_{max} and K , $Ca_{max} \sim K^{-1}$.

4. Conclusions and remarks

From the perspective of kinetic theory, the transport properties of a flowing system are described by the distribution function f or by the full sequence of its kinetic moments. The conservative kinetic moments of f include the density, momentum and energy. Acquisition of these conservative kinetic moments is equivalent to knowing only the equilibrium distribution function $f^{(0)}$, namely perfect fluids free from dissipative effects. How and to what extent the system deviates from the thermodynamic equilibrium remains completely unknown at this stage.

To know the distribution function f is equivalent to knowing all the kinetic moments of f , which is neither possible nor necessary for the vast majority of situations. Which kinetic moments need to be known for multi-scale modelling of complex flows is the first key question that the DBM endeavours to address. The second is how to detect, describe, present and analyse THNE states. Along this line, we present a framework for constructing multi-scale discrete Boltzmann models for thermal multiphase flows ranging from continuum to transition flow regimes. The DBM is a straightforward and efficient kinetic moment-matching method, for bulk flow, whose basic framework consists of three fundamental steps: (i) establishment of the formal links with the modified continuous Boltzmann–BGK equation, the extended hydrodynamic equations and the sought thermo-hydrodynamic non-equilibrium (THNE) phenomena under consideration; (ii) formulation of the THNE measures; and (iii) discretization of the particle velocity space for the construction of the discrete equilibrium distribution function. In addition, phase space manifolds spanned by the independent components of non-conservative kinetic moments of $(f - f^{(0)})$ are introduced to describe the corresponding non-equilibrium states and effects. The concept of metric distance from the origin in such phase space is extended to describe intuitively the non-equilibrium depth. The concept of metric distance between two points in such phase space is extended to describe intuitively the difference between two states. For near-wall flow, one more step, construction of kinetic boundary conditions, is needed.

In the case of the validity of Chapman–Enskog theory, step (ii) permits us to select the minimum physical requirements for describing the THNE quantities of interest to the desired order of accuracy, that is, it determines the fewest required kinetic moments $\Phi_n = (M_0, M_1, \dots, M_n)^T$ that the discrete equilibrium distribution function should retrieve during the coarse-grained physical modelling process. It also provides valuable byproducts: higher-order constitutive relations and the most relevant higher-order THNE manifestations that are expected to improve the macroscopic modelling and enhance the understanding of dynamic constitutive relations.

The set of the fewest kinetic moments offers a unique perspective to investigate the non-equilibrium behaviour of the ‘mesoscale’ or ‘dilemma’ situations where the continuum modelling fails and the molecular dynamics method lacks sufficient power to reach up to the scales of interest. The research perspective and modelling accuracy depend on the specific elements of moment sets, and can be adjusted and improved in time. For instance, to access stronger non-equilibrium effects, one needs to include more higher-order moment relations into Φ_n , so that the discrete Boltzmann model becomes more consistent with the continuous Boltzmann equation far from equilibrium.

Importantly, the computational complexity of the DBM increases only mildly in the process, as opposed to the case of generalized hydrodynamics, such as the Burnett or the super-Burnett equations.

As model examples, two-dimensional discrete Boltzmann models with 13, 15 and 30 discrete velocities at Navier–Stokes and beyond Burnett levels have been proposed and evaluated. It is found that the incorporation of additional higher-order kinetic moments helps to enhance the liquid–vapour density ratio that the model can hold, to curb spurious currents around the interface, and to ensure better mass, momentum and energy conservation in phase-separating systems. The multi-scale predictive capability of the discrete Boltzmann model to describe THNE features increases with the number of independent kinetic moments included by the model. As fast-varying variables, the thermodynamic and THNE measures provide more detailed information on the non-equilibrium multiphase flow system than methods based on macroscopic conserved quantities alone, thereby shedding new light on these complex states of flowing matter far from equilibrium. For example, the present work helps in preparing the cognitive basis for subsequent experimental research, and provides theoretical guidance for further experimental design, observation and analysis.

Future work includes: a more complete comparison among DBM results, high-order moment method (Struchtrup & Frezzotti 2022), particle-based method (Frezzotti *et al.* 2018, 2019) and experimental results; the incorporation of the external force in a more fundamental way; the construction of appropriate kinetic boundary conditions (Struchtrup *et al.* 2017; Zhang *et al.* 2022*b*); and consideration of the case with faster phase separation, say the phase transition time scale is comparable to the molecular thermal relaxation.

Acknowledgements. The authors sincerely thank the anonymous reviewers for their valuable and instructive comments and suggestions, which were very helpful for revising the manuscript. Also, we warmly thank Dr T. Chen (Southern University of Science and Technology), Dr Y. Zhang (Zhengzhou University), Dr C. Lin (Sun Yat-sen University), Dr D. Zhang (China University of Mining and Technology (Beijing)) and Dr B. Chen (North China Institute of Aerospace Engineering) for many helpful discussions.

Funding. We acknowledge support from the National Natural Science Foundation of China (grant nos 11875001 and 12172061), the Natural Science Foundation of Hebei Province (grant nos. A2021409001 and 226Z7601G), the ‘Three, Three and Three’ Talent Project of Hebei Province (grant no. A202105005), the Natural Science Foundation of Fujian Province (grant no. 2021J01652), the CAEP Foundation (grant no. CX2019033), the opening project of State Key Laboratory of Explosion Science and Technology (Beijing Institute of Technology) (grant no. KFJJ21-16M) and the Foundation of Laboratory of Computational Physics. S.S. gratefully acknowledges financial support from the European Research Council under the Horizon 2020 Programme Grant Agreement no. 739964 (‘COPMAT’).

Declaration of interests. The authors report no conflict of interest.

Author ORCIDs.

 Yanbiao Gan <https://orcid.org/0000-0002-0191-9022>;

 Aiguo Xu <https://orcid.org/0000-0002-6179-5973>;

 Huilin Lai <https://orcid.org/0000-0001-5978-5736>;

 Sauro Succi <https://orcid.org/0000-0002-3070-3079>.

Appendix A. Determination of the relations among THNE and TNE measures

According to the definitions in (2.9) and (2.10), $\Delta_{m,n}$ describes the combination effects of thermodynamic non-equilibrium (TNE) and hydrodynamic non-equilibrium (HNE), which are usually called the thermo-hydrodynamic non-equilibrium (THNE) effects; $\Delta_{m,n}^*$

reflects molecular individualism on top of organized collective motion, describing only the TNE effects. Next, we list the relations among them:

$$\begin{aligned}
 \Delta_2^* &= M_2^*(f - f^{(0)}) = \int_{-\infty}^{\infty} (f - f^{(0)}) \mathbf{v}^* \mathbf{v}^* d\mathbf{v} \\
 &= \int_{-\infty}^{\infty} (f - f^{(0)}) (\mathbf{v} - \mathbf{u})(\mathbf{v} - \mathbf{u}) d\mathbf{v} \\
 &= \int_{-\infty}^{\infty} (f - f^{(0)}) (\mathbf{v}\mathbf{v} - \mathbf{v}\mathbf{u} - \mathbf{u}\mathbf{v} + \mathbf{u}\mathbf{u}) d\mathbf{v} \\
 &= \Delta_2 - \int_{-\infty}^{\infty} (f - f^{(0)}) \mathbf{v}\mathbf{u} d\mathbf{v} - \int_{-\infty}^{\infty} (f - f^{(0)}) \mathbf{u}\mathbf{v} d\mathbf{v} + \int_{-\infty}^{\infty} (f - f^{(0)}) \mathbf{u}\mathbf{u} d\mathbf{v} \\
 &= \Delta_2 - \left[\int_{-\infty}^{\infty} (f - f^{(0)}) \mathbf{v} d\mathbf{v} \right] \mathbf{u} - \mathbf{u} \left[\int_{-\infty}^{\infty} (f - f^{(0)}) \mathbf{v} d\mathbf{v} \right] + \left[\int_{-\infty}^{\infty} (f - f^{(0)}) d\mathbf{v} \right] \mathbf{u}\mathbf{u}.
 \end{aligned} \tag{A1}$$

It is well known that $\int_{-\infty}^{\infty} (f - f^{(0)}) d\mathbf{v} = 0$ and $\int_{-\infty}^{\infty} (f - f^{(0)}) \mathbf{v} d\mathbf{v} = 0$, so

$$\Delta_2^* = \Delta_2. \tag{A2}$$

We have

$$\begin{aligned}
 \Delta_{3,1}^* &= M_{3,1}^*(f - f^{(0)}) = \int_{-\infty}^{\infty} (f - f^{(0)}) \mathbf{v}^* \frac{\mathbf{v}^* \cdot \mathbf{v}^*}{2} d\mathbf{v} \\
 &= \int_{-\infty}^{\infty} (f - f^{(0)}) (\mathbf{v} - \mathbf{u}) \frac{v^2 - 2\mathbf{v} \cdot \mathbf{u} + u^2}{2} d\mathbf{v} \\
 &= \int_{-\infty}^{\infty} (f - f^{(0)}) \mathbf{v} \frac{v^2 - 2\mathbf{v} \cdot \mathbf{u} + u^2}{2} d\mathbf{v} - \int_{-\infty}^{\infty} (f - f^{(0)}) \mathbf{u} \frac{v^2 - 2\mathbf{v} \cdot \mathbf{u} + u^2}{2} d\mathbf{v}.
 \end{aligned} \tag{A3}$$

It is clear that $\int_{-\infty}^{\infty} (f - f^{(0)}) (v^2/2) d\mathbf{v} = 0$, hence

$$\begin{aligned}
 \Delta_{3,1}^* &= \int_{-\infty}^{\infty} (f - f^{(0)}) \mathbf{v} \left(\frac{v^2}{2} - \mathbf{v} \cdot \mathbf{u} + \frac{u^2}{2} \right) d\mathbf{v} \\
 &= \Delta_{3,1} - \int_{-\infty}^{\infty} (f - f^{(0)}) \mathbf{v} \left(\mathbf{v} \cdot \mathbf{u} - \frac{u^2}{2} \right) d\mathbf{v} \\
 &= \Delta_{3,1} - \left[\int_{-\infty}^{\infty} (f - f^{(0)}) \mathbf{v}\mathbf{v} d\mathbf{v} \right] \cdot \mathbf{u} \\
 &= \Delta_{3,1} - \Delta_2^* \cdot \mathbf{u}.
 \end{aligned} \tag{A4}$$

Similarly,

$$\begin{aligned}
 \Delta_3^* &= M_3^*(f - f^{(0)}) = \int_{-\infty}^{\infty} (f - f^{(0)}) \mathbf{v}^* \mathbf{v}^* \mathbf{v}^* d\mathbf{v} \\
 &= \int_{-\infty}^{\infty} (f - f^{(0)}) (\mathbf{v} - \mathbf{u})(\mathbf{v} - \mathbf{u})(\mathbf{v} - \mathbf{u}) d\mathbf{v}
 \end{aligned}$$

DB multi-scale modelling of non-equilibrium multiphase flows

$$\begin{aligned}
 &= \int_{-\infty}^{\infty} (f - f^{(0)})(\mathbf{v}\mathbf{v}\mathbf{v} - \mathbf{v}\mathbf{u}\mathbf{v} - \mathbf{u}\mathbf{v}\mathbf{v} + \mathbf{u}\mathbf{v}\mathbf{u} - \mathbf{v}\mathbf{v}\mathbf{u} + \mathbf{v}\mathbf{u}\mathbf{u} + \mathbf{u}\mathbf{v}\mathbf{u} - \mathbf{u}\mathbf{u}\mathbf{u}) \, d\mathbf{v} \\
 &= \int_{-\infty}^{\infty} (f - f^{(0)})(\mathbf{v}\mathbf{v}\mathbf{v} - \mathbf{v}\mathbf{u}\mathbf{v} - \mathbf{u}\mathbf{v}\mathbf{v} - \mathbf{v}\mathbf{v}\mathbf{u}) \, d\mathbf{v} \\
 &= \mathbf{\Delta}_3 - \int_{-\infty}^{\infty} (f - f^{(0)})(\mathbf{v}\mathbf{u}\mathbf{v} + \mathbf{u}\mathbf{v}\mathbf{v} + \mathbf{v}\mathbf{v}\mathbf{u}) \, d\mathbf{v} \\
 &= \mathbf{\Delta}_3 - \int_{-\infty}^{\infty} (f - f^{(0)})\mathbf{v}\mathbf{u}\mathbf{v} \, d\mathbf{v} - \mathbf{u}\mathbf{\Delta}_2^* - \mathbf{\Delta}_2^*\mathbf{u} \\
 &= \mathbf{\Delta}_3 - (u_\alpha \mathbf{\Delta}_{2\beta\gamma}^* + u_\beta \mathbf{\Delta}_{2\alpha\gamma}^* + u_\gamma \mathbf{\Delta}_{2\alpha\beta}^*)\mathbf{e}_\alpha \mathbf{e}_\beta \mathbf{e}_\gamma
 \end{aligned} \tag{A5}$$

and

$$\begin{aligned}
 \mathbf{\Delta}_{4,2}^* &= \mathbf{M}_{4,2}^*(f - f^{(0)}) = \int_{-\infty}^{\infty} (f - f^{(0)})\mathbf{v}^*\mathbf{v}^* \frac{\mathbf{v}^* \cdot \mathbf{v}^*}{2} \, d\mathbf{v} \\
 &= \int_{-\infty}^{\infty} (f - f^{(0)})(\mathbf{v} - \mathbf{u})(\mathbf{v} - \mathbf{u}) \left(\frac{v^2}{2} - \mathbf{v} \cdot \mathbf{u} + \frac{u^2}{2} \right) \, d\mathbf{v} \\
 &= \int_{-\infty}^{\infty} (f - f^{(0)})(\mathbf{v}\mathbf{v} - \mathbf{v}\mathbf{u} - \mathbf{u}\mathbf{v} + \mathbf{u}\mathbf{u}) \left(\frac{v^2}{2} - \mathbf{v} \cdot \mathbf{u} + \frac{u^2}{2} \right) \, d\mathbf{v} \\
 &= \int_{-\infty}^{\infty} (f - f^{(0)})(\mathbf{v}\mathbf{v} - \mathbf{v}\mathbf{u} - \mathbf{u}\mathbf{v}) \left(\frac{v^2}{2} - \mathbf{v} \cdot \mathbf{u} + \frac{u^2}{2} \right) \, d\mathbf{v} \\
 &= \int_{-\infty}^{\infty} (f - f^{(0)}) \left(\mathbf{v}\mathbf{v} \frac{v^2}{2} - \mathbf{v}\mathbf{u} \frac{v^2}{2} - \mathbf{u}\mathbf{v} \frac{v^2}{2} \right) \, d\mathbf{v} \\
 &\quad - \int_{-\infty}^{\infty} (f - f^{(0)})(\mathbf{v}\mathbf{v}\mathbf{v} \cdot \mathbf{u} - \mathbf{v}\mathbf{u}\mathbf{v} \cdot \mathbf{u} - \mathbf{u}\mathbf{v}\mathbf{v} \cdot \mathbf{u}) \, d\mathbf{v} + \int_{-\infty}^{\infty} (f - f^{(0)})\mathbf{v}\mathbf{v} \frac{u^2}{2} \, d\mathbf{v} \\
 &= \mathbf{\Delta}_{4,2} - \mathbf{\Delta}_{3,1}\mathbf{u} - \mathbf{u}\mathbf{\Delta}_{3,1} - \mathbf{\Delta}_3 \cdot \mathbf{u} + \int_{-\infty}^{\infty} (f - f^{(0)})(\mathbf{v}\mathbf{u}\mathbf{v} \cdot \mathbf{u}) \, d\mathbf{v} + \mathbf{u}\mathbf{\Delta}_2 \cdot \mathbf{u} + \frac{u^2}{2} \mathbf{\Delta}_2 \\
 &= \mathbf{\Delta}_{4,2} - (\mathbf{\Delta}_{3,1}^* + \mathbf{\Delta}_2^* \cdot \mathbf{u})\mathbf{u} - \mathbf{u}(\mathbf{\Delta}_{3,1}^* + \mathbf{\Delta}_2^* \cdot \mathbf{u}) \\
 &\quad - \left[\mathbf{\Delta}_3^* + \int_{-\infty}^{\infty} (f - f^{(0)})\mathbf{v}\mathbf{u}\mathbf{v} \, d\mathbf{v} + \mathbf{u}\mathbf{\Delta}_2^* + \mathbf{\Delta}_2^*\mathbf{u} \right] \cdot \mathbf{u} \\
 &\quad + \int_{-\infty}^{\infty} (f - f^{(0)})(\mathbf{v}\mathbf{u}\mathbf{v} \cdot \mathbf{u}) \, d\mathbf{v} + \mathbf{u}\mathbf{\Delta}_2 \cdot \mathbf{u} + \frac{u^2}{2} \mathbf{\Delta}_2 \\
 &= \mathbf{\Delta}_{4,2} - \mathbf{\Delta}_{3,1}^*\mathbf{u} - \mathbf{u}\mathbf{\Delta}_{3,1}^* - \mathbf{\Delta}_3^* \cdot \mathbf{u} - \mathbf{\Delta}_2^* \cdot \mathbf{u}\mathbf{u} - \mathbf{u}\mathbf{\Delta}_2^* \cdot \mathbf{u} - \frac{u^2}{2} \mathbf{\Delta}_2^*.
 \end{aligned} \tag{A6}$$

Appendix B. Expressions for the first- and second-order TNE measures

	$\Delta_{2xx}^{*(1)} = -\rho T \tau A_{1,-1}$
$\Delta_{2\alpha\beta}^{*(1)}$	$\Delta_{2xy}^{*(1)} = -\rho T \tau a_{1,1}$ $\Delta_{2yy}^{*(1)} = -\Delta_{2xx}^{*(1)}$
$\Delta_{3,1\alpha}^{*(1)}$	$\Delta_{3,1x}^{*(1)} = -2\rho T \tau \partial_x T$ $\Delta_{3,1y}^{*(1)} = -2\rho T \tau \partial_y T$
$\Delta_{3\alpha\beta\gamma}^{*(1)}$	$\Delta_{3xxx}^{*(1)} = -3\rho T \tau \partial_x T$ $\Delta_{3xxy}^{*(1)} = -\rho T \tau \partial_y T$ $\Delta_{3xyy}^{*(1)} = -\rho T \tau \partial_x T$ $\Delta_{3yyy}^{*(1)} = -3\rho T \tau \partial_y T$
$\Delta_{4,2\alpha\beta}^{*(1)}$	$\Delta_{4,2xx}^{*(1)} = -3\rho T^2 \tau A_{1,-1}$ $\Delta_{4,2xy}^{*(1)} = -3\rho T^2 \tau a_{1,1}$ $\Delta_{4,2yy}^{*(1)} = -\Delta_{4,2xx}^{*(1)}$
$\Delta_{2\alpha\beta}^{*(2)}$	$\Delta_{2xx}^{*2}/\tau^2 = -(2C_1 A_{1,-1} + B_{1,-1})\rho T^2 - [D_{1,-1} + \Gamma(u_x)_{1,-1} + \Gamma(u_y)_{1,-1}]\rho T$ $-T^2 F(\rho)_{1,-1} + \rho \Gamma(T)_{1,-1} + \frac{T^2}{\rho} \Gamma(\rho)_{1,-1}$ $\Delta_{2xy}^{*2}/\tau^2 = -(2C_1 a_{1,1} + b_{1,1})\rho T^2 - (d_{1,1} + 2E_{1,1})\rho T$ $-2T^2 \lambda(\rho) + 2\rho \theta(T) + \frac{2T^2}{\rho} \theta(\rho)$ $\Delta_{2yy}^{*(2)} = -\Delta_{2xx}^{*(2)}$
$\Delta_{3,1\alpha}^{*(2)}$	$\Delta_{3,1x}^{*2}/\tau^2 = -4\rho T^3 \partial_x C_1 - [A_{1,-1} B_x + a_{1,1} B_y + 12C_1 \partial_x T + F(u_x)_{1,-1} + 2\lambda(u_y)]\rho T^2 + (A_{1,-3} \partial_x T + a_{1,3} \partial_y T) 2\rho T$ $\Delta_{3,1y}^{*2}/\tau^2 = -4\rho T^3 \partial_y C_1 - [a_{1,1} B_x - A_{1,-1} B_y + 12C_1 \partial_y T - F(u_y)_{1,-1} + 2\lambda(u_x)]\rho T^2 + (a_{3,1} \partial_x T + A_{-3,1} \partial_y T) 2\rho T$
$\Delta_{3\alpha\beta\gamma}^{*(2)}$	$\Delta_{3xxx}^{*2}/\tau^2 = -6\rho T^3 \partial_x C_1 - [A_{1,-1} B_x + 6C_1 \partial_x T + 2\lambda(u_y)] 3\rho T^2 + (A_{1,-2} \partial_x T + \partial_y u_x \partial_y T) 6\rho T$ $\Delta_{3yyy}^{*2}/\tau^2 = -6\rho T^3 \partial_y C_1 - [A_{-1,1} B_y + 6C_1 \partial_y T + 2\lambda(u_x)] 3\rho T^2 + (A_{-2,1} \partial_y T + \partial_x u_y \partial_x T) 6\rho T$ $\Delta_{3xxy}^{*(2)} = 2\Delta_{3,1y}^{*(2)} - \Delta_{3yyy}^{*(2)}$ $\Delta_{3xyy}^{*(2)} = 2\Delta_{3,1x}^{*(2)} - \Delta_{3xxx}^{*(2)}$
$\Delta_{4,2\alpha\beta}^{*(2)}$	$\Delta_{4,2xx}^{*2}/\tau^2 = -(4C_1 A_{1,-1} + B_{1,-1}) 3\rho T^3 - [D_{10,-2} + \Gamma(u_x)_{1,-5} + \Gamma(u_y)_{1,-5} + 4e_{1,-1} - F(T)_{7,1}]\rho T^2 + 3\rho T \Gamma(T)_{7,1} - 3T^3 F(\rho)_{1,-1} + \frac{3T^3}{\rho} \Gamma(\rho)_{1,-1}$ $\Delta_{4,2xy}^{*2}/\tau^2 = -(4C_1 a_{11} + b_{1,1}) 3\rho T^3 - [d_{1,1} + E_{1,1} - \lambda(T)] 6\rho T^2 + 18\rho T \theta(T) - 6T^3 \lambda(\rho) + \frac{6T^3}{\rho} \theta(\rho)$ $\Delta_{4,2yy}^{*2}/\tau^2 = (4C_1 A_{1,-1} + B_{1,-1}) 3\rho T^3 + [D_{2,-10} + \Gamma(u_x)_{5,-1} + \Gamma(u_y)_{5,-1} + 4e_{-1,1} + F(T)_{1,7}]\rho T^2 + 3\rho T \Gamma(T)_{1,7} + 3T^3 F(\rho)_{1,-1} - \frac{3T^3}{\rho} \Gamma(\rho)_{1,-1}$

DB multi-scale modelling of non-equilibrium multiphase flows

Here, $A_{m,n} = m\partial_x u_x + n\partial_y u_y$, $a_{m,n} = m\partial_x u_y + m\partial_y u_x$, $B_{m,n} = m\partial_x B_x + n\partial_y B_y$, $b_{m,n} = m\partial_x B_y + n\partial_y B_x$, $D_{m,n} = mB_x\partial_x T + nB_y\partial_y T$, $d_{m,n} = mB_y\partial_x T + nB_x\partial_y T$, $E_{m,n} = m\partial_x u_x\partial_y u_x + n\partial_x u_y\partial_y u_y$, $e_{m,n} = m\partial_x u_x\partial_y u_y + n\partial_x u_y\partial_y u_x$, $\theta(\cdot) = \partial_x(\cdot)\partial_y(\cdot)$, $\lambda(\cdot) = (\partial^2/\partial y\partial x)(\cdot)$, $F(\cdot)_{m,n} = m(\partial^2/\partial x^2)(\cdot) + n(\partial^2/\partial y^2)(\cdot)$, $\Gamma(\cdot)_{m,n} = m[\partial_x(\cdot)]^2 + n[\partial_y(\cdot)]^2$, $C_1 = C + C_q$.

Appendix C. Independent kinetic moments required to fully characterize the first- and second-order TNE measures

M_m	Independent kinetic moments
M_0	$M_0 = \rho$
M_1	$M_{1x} = \rho u_x$ $M_{1y} = \rho u_y$
M_2	$M_{2xx} = \rho(T + u_x^2)$ $M_{2xy} = \rho u_x u_y$ $M_{2yy} = \rho(T + u_y^2)$
M_3	$M_{3xxx} = \rho u_x(3T + u_x^2)$ $M_{3xxy} = \rho u_y(T + u_x^2)$ $M_{3xyy} = \rho u_x(T + u_y^2)$ $M_{3yyy} = \rho u_y(3T + u_y^2)$
M_4	$M_{4xxxx} = \rho(3T^2 + 6Tu_x^2 + u_x^4)$ $M_{4xxy} = \rho u_x u_y(3T + u_x^2)$ $M_{4xyy} = \rho(T + u_x^2)(T + u_y^2)$ $M_{4yyy} = \rho u_x u_y(3T + u_y^2)$ $M_{4yyyy} = \rho(3T^2 + 6Tu_y^2 + u_y^4)$
M_5	$M_{5xxxxx} = \rho u_x(15T^2 + 10Tu_x^2 + u_x^4)$ $M_{5xxxxy} = \rho u_y(3T^2 + 6Tu_x^2 + u_x^4)$ $M_{5xxxyy} = \rho u_x(3T + u_x^2)(T + u_y^2)$ $M_{5xxyyy} = \rho u_y(3T + u_y^2)(T + u_x^2)$ $M_{5xyyyy} = \rho u_x(3T^2 + 6Tu_y^2 + u_y^4)$ $M_{5yyyyy} = \rho u_y(15T^2 + 10Tu_y^2 + u_y^4)$
$M_{6,4}$	$M_{6,4xxxx} = \frac{1}{2}\rho[18T^3 + 3T^2(u^2 + 16u_x^2) + 2Tu_x^2(3u^2 + 5u_x^2) + u^2u_x^4]$ $M_{6,4xxy} = \frac{1}{2}\rho u_x u_y[24T^2 + T(3u^2 + 10u_x^2) + u^2u_x^2]$ $M_{6,4xyy} = \frac{1}{2}\rho[6T^3 + Tu^2(9T + u^2) + u_x^2u_y^2(10T + u^2)]$ $M_{6,4xyyy} = \frac{1}{2}\rho u_x u_y[24T^2 + T(3u^2 + 10u_y^2) + u^2u_y^2]$ $M_{6,4yyyy} = \frac{1}{2}\rho[18T^3 + 3T^2(u^2 + 16u_y^2) + 2Tu_y^2(3u^2 + 5u_y^2) + u^2u_y^4]$
$M_{7,3}$	$M_{7,3xxx} = \frac{1}{2}\rho u_x[144T^3 + 16T^2(3u^2 + 5u_x^2) + Tu^2(3u^2 + 20u_x^2) + u^4u_x^2]$ $M_{7,3xxy} = \frac{1}{2}\rho u_y[48T^3 + 16T^2(u^2 + 5u_x^2) + Tu^2(u^2 + 20u_x^2) + u^4u_x^2]$ $M_{7,3xyy} = \frac{1}{2}\rho u_x[48T^3 + 16T^2(u^2 + 5u_y^2) + Tu^2(u^2 + 20u_y^2) + u^4u_y^2]$ $M_{7,3yyy} = \frac{1}{2}\rho u_y[144T^3 + 16T^2(3u^2 + 5u_y^2) + Tu^2(3u^2 + 20u_y^2) + u^4u_y^2]$

REFERENCES

AARTS, D.G.A.L., SCHMIDT, M. & LEKKERKERKER, H.N.W. 2004 Direct visual observation of thermal capillary waves. *Science* **304** (5672), 847–850.

- AMBRUŞ, V.E., BUSUIOC, S., WAGNER, A.J., PAILLUSSON, F. & KUSUMAATMAJA, H. 2019 Multicomponent flow on curved surfaces: a vielbein lattice Boltzmann approach. *Phys. Rev. E* **100** (6), 063306.
- AMBRUŞ, V.E. & SOFONEA, V. 2016 Lattice Boltzmann models based on half-range Gauss–Hermite quadratures. *J. Comput. Phys.* **316**, 760–788.
- ANSUMALI, S., KARLIN, I.V., ARCIDIACONO, S., ABBAS, A. & PRASIANAKIS, N.I. 2007 Hydrodynamics beyond Navier–Stokes: exact solution to the lattice Boltzmann hierarchy. *Phys. Rev. Lett.* **98** (12), 124502.
- BAO, Y., QIU, R., ZHOU, K., ZHOU, T., WENG, Y., LIN, K. & YOU, Y. 2022 Study of shock wave/boundary layer interaction from the perspective of nonequilibrium effects. *Phys. Fluids* **34** (4), 046109.
- BEDAUX, D. 1986 Nonequilibrium thermodynamics and statistical physics of surfaces. *Adv. Chem. Phys.* **64**, 47–109.
- BENZI, R., BIFERALE, L., SBRAGAGLIA, M., SUCCI, S. & TOSCHI, F. 2006 Mesoscopic two-phase model for describing apparent slip in micro-channel flows. *Europhys. Lett.* **74** (4), 651.
- BENZI, R., SUCCI, S. & VERGASSOLA, M. 1992 The lattice Boltzmann equation: theory and applications. *Phys. Rep.* **222** (3), 145–197.
- BERNASCHI, M., MELCHIONNA, S. & SUCCI, S. 2019 Mesoscopic simulations at the physics–chemistry–biology interface. *Rev. Mod. Phys.* **91** (2), 025004.
- BHAIRAPURADA, K., DENET, B. & BOIVIN, P. 2022 A lattice-Boltzmann study of premixed flames thermo-acoustic instabilities. *Combust. Flame* **240**, 112049.
- BHATNAGAR, P.L., GROSS, E.P. & KROOK, M. 1954 A model for collision processes in gases. I. Small amplitude processes in charged and neutral one-component systems. *Phys. Rev.* **94** (3), 511.
- BIFERALE, L., PERLEKAR, P., SBRAGAGLIA, M. & TOSCHI, F. 2012 Convection in multiphase fluid flows using lattice Boltzmann methods. *Phys. Rev. Lett.* **108** (10), 104502.
- BRENNEN, C.E. 2005 *Fundamentals of Multiphase Flow*. Cambridge University Press.
- BU, W., KIM, D. & VAKNIN, D. 2014 Density profiles of liquid/vapor interfaces away from their critical points. *J. Phys. Chem. C* **118** (23), 12405–12409.
- BUSUIOC, S., AMBRUŞ, V.E., BICIUŞCĂ, T. & SOFONEA, V. 2020 Two-dimensional off-lattice Boltzmann model for van der Waals fluids with variable temperature. *Comput. Maths Applics.* **79** (1), 111–140.
- CARENZA, L.N., GONNELLA, G., MARENDUZZO, D. & NEGRO, G. 2019 Rotation and propulsion in 3D active chiral droplets. *Proc. Natl Acad. Sci.* **116** (44), 22065–22070.
- CARNAHAN, N.F. & STARLING, K.E. 1969 Equation of state for nonattracting rigid spheres. *J. Chem. Phys.* **51** (2), 635–636.
- CATES, M.E., FIELDING, S.M., MARENDUZZO, D., ORLANDINI, E. & YEOMANS, J.M. 2008 Shearing active gels close to the isotropic–nematic transition. *Phys. Rev. Lett.* **101** (6), 068102.
- CHAI, Z., HUANG, C., SHI, B. & GUO, Z. 2016 A comparative study on the lattice Boltzmann models for predicting effective diffusivity of porous media. *Intl J. Heat Mass Transfer* **98**, 687–696.
- CHAI, Z., LIANG, H., DU, R. & SHI, B. 2019 A lattice Boltzmann model for two-phase flow in porous media. *SIAM J. Sci. Comput.* **41** (4), B746–B772.
- CHAI, Z. & SHI, B. 2008 A novel lattice Boltzmann model for the Poisson equation. *Appl. Math. Model.* **32** (10), 2050–2058.
- CHAPMAN, S. & COWLING, T.G. 1990 *The Mathematical Theory of Non-Uniform Gases: An Account of the Kinetic Theory of Viscosity, Thermal Conduction and Diffusion in Gases*. Cambridge University Press.
- CHEN, X., CHAI, Z., SHANG, J. & SHI, B. 2021b Multiple-relaxation-time finite-difference lattice Boltzmann model for the nonlinear convection–diffusion equation. *Phys. Rev. E* **104** (3), 035308.
- CHEN, Y. & DENG, Z. 2017 Hydrodynamics of a droplet passing through a microfluidic T-junction. *J. Fluid Mech.* **819**, 401–434.
- CHEN, S. & DOOLEN, G.D. 1998 Lattice Boltzmann method for fluid flows. *Annu. Rev. Fluid Mech.* **30** (1), 329–364.
- CHEN, L., KANG, Q., TANG, Q., ROBINSON, B.A., HE, Y. & TAO, W. 2015 Pore-scale simulation of multicomponent multiphase reactive transport with dissolution and precipitation. *Intl J. Heat Mass Transfer* **85**, 935–949.
- CHEN, L., KANG, Q. & TAO, W. 2021a Pore-scale numerical study of multiphase reactive transport processes in cathode catalyst layers of proton exchange membrane fuel cells. *Intl J. Hydrogen Energy* **46** (24), 13283–13297.
- CHEN, Z., SHU, C., YANG, L.M., ZHAO, X. & LIU, N.Y. 2021c Phase-field-simplified lattice Boltzmann method for modeling solid–liquid phase change. *Phys. Rev. E* **103** (2), 023308.
- CHEN, T., WU, L., WANG, L. & CHEN, S. 2022b Rarefaction effects in head-on collision of two identical droplets. Preprint. [arXiv:2205.03604](https://arxiv.org/abs/2205.03604).

- CHEN, F., XU, A., ZHANG, Y., GAN, Y., LIU, B. & WANG, S. 2022a Delineation of the flow and mixing induced by Rayleigh–Taylor instability through tracers. *Front. Phys.* **17** (3), 33505.
- CHEN, F., XU, A., ZHANG, Y. & ZENG, Q. 2020 Morphological and non-equilibrium analysis of coupled Rayleigh–Taylor–Kelvin–Helmholtz instability. *Phys. Fluids* **32** (10), 104111.
- CHEN, Q., ZHANG, X. & ZHANG, J. 2013 Improved treatments for general boundary conditions in the lattice Boltzmann method for convection–diffusion and heat transfer processes. *Phys. Rev. E* **88** (3), 033304.
- CHEN, W.F., ZHAO, W.W., JIANG, Z.Z. & LIUI, H.L. 2016 A review of moment equations for rarefied gas dynamics. *Phys. Gases* **1** (5), 9–24.
- CHEN, X., ZHONG, C. & YUAN, X. 2011 Lattice Boltzmann simulation of cavitating bubble growth with large density ratio. *Comput. Maths Applics.* **61** (12), 3577–3584.
- CHIKATAMARLA, S.S., ANSUMALI, S. & KARLIN, I.V. 2006 Grad’s approximation for missing data in lattice Boltzmann simulations. *Europhys. Lett.* **74** (2), 215.
- CHIKATAMARLA, S.S. & KARLIN, I.V. 2009 Lattices for the lattice Boltzmann method. *Phys. Rev. E* **79** (4), 046701.
- COCLITE, A., GONNELLA, G. & LAMURA, A. 2014 Pattern formation in liquid–vapor systems under periodic potential and shear. *Phys. Rev. E* **89** (6), 063303.
- CORBERI, F., GONNELLA, G. & LAMURA, A. 1998 Spinodal decomposition of binary mixtures in uniform shear flow. *Phys. Rev. Lett.* **81** (18), 3852.
- COREIXAS, C., WISSOCQ, G., PUIGT, G., BOUSSUGE, J. & SAGAUT, P. 2017 Recursive regularization step for high-order lattice Boltzmann methods. *Phys. Rev. E* **96** (3), 033306.
- CZELUSNIAK, L.E., MAPELLI, V.P., GUZELLA, M.S., CABEZAS-GÓMEZ, L. & WAGNER, A.J. 2020 Force approach for the pseudopotential lattice Boltzmann method. *Phys. Rev. E* **102** (3), 033307.
- DAI, R., LI, W., MOSTAGHIMI, J., WANG, Q. & ZENG, M. 2020 On the optimal heat source location of partially heated energy storage process using the newly developed simplified enthalpy based lattice Boltzmann method. *Appl. Energy* **275**, 115387.
- DOOSTMOHAMMADI, A., ADAMER, M.F., THAMPI, S.P. & YEOMANS, J.M. 2016 Stabilization of active matter by flow-vortex lattices and defect ordering. *Nat. Commun.* **7** (1), 10557.
- DU, R. & LIU, Z. 2020 A lattice Boltzmann model for the fractional advection–diffusion equation coupled with incompressible Navier–Stokes equation. *Appl. Math. Lett.* **101**, 106074.
- DUAN, Y. & LIU, R. 2007 Lattice Boltzmann model for two-dimensional unsteady Burgers’ equation. *J. Comput. Appl. Maths* **206** (1), 432–439.
- DUPIN, M., HALLIDAY, I. & CARE, C. 2006 A multi-component lattice Boltzmann scheme: towards the mesoscale simulation of blood flow. *Med. Engng Phys.* **28** (1), 13–18.
- ELTON, B.H. 1996 Comparisons of lattice Boltzmann and finite difference methods for a two-dimensional viscous Burgers equation. *SIAM J. Sci. Comput.* **17** (4), 783–813.
- EVANS, R. 1979 The nature of the liquid–vapour interface and other topics in the statistical mechanics of non-uniform, classical fluids. *Adv. Phys.* **28** (2), 143–200.
- FAKHARI, A. & LEE, T. 2013 Multiple-relaxation-time lattice Boltzmann method for immiscible fluids at high Reynolds numbers. *Phys. Rev. E* **87** (2), 023304.
- FALCUCCI, G., AMATI, G., FANELLI, P., KRASSTEV, V.K., POLVERINO, G., PORFIRI, M. & SUCCI, S. 2021 Extreme flow simulations reveal skeletal adaptations of deep-sea sponges. *Nature* **595** (7868), 537–541.
- FALCUCCI, G., CHIATTI, G., SUCCI, S., MOHAMAD, A.A. & KUZMIN, A. 2009 Rupture of a ferrofluid droplet in external magnetic fields using a single-component lattice Boltzmann model for nonideal fluids. *Phys. Rev. E* **79** (5), 056706.
- FALCUCCI, G., JANNELLI, E., UBERTINI, S. & SUCCI, S. 2013 Direct numerical evidence of stress-induced cavitation. *J. Fluid Mech.* **728**, 362–375.
- FEI, L., QIN, F., WANG, G., LUO, K.H., DEROME, D. & CARMELIET, J. 2022 Droplet evaporation in finite-size systems: theoretical analysis and mesoscopic modeling. *Phys. Rev. E* **105** (2), 025101.
- FEI, L., YANG, J., CHEN, Y., MO, H. & LUO, K.H. 2020 Mesoscopic simulation of three-dimensional pool boiling based on a phase-change cascaded lattice Boltzmann method. *Phys. Fluids* **32** (10), 103312.
- FREZZOTTI, A. 2011 Boundary conditions at the vapor–liquid interface. *Phys. Fluids* **23** (3), 030609.
- FREZZOTTI, A., BARBANTE, P. & GIBELLI, L. 2019 Direct simulation Monte Carlo applications to liquid–vapor flows. *Phys. Fluids* **31** (6), 062103.
- FREZZOTTI, A., GIBELLI, L., LOCKERBY, D.A. & SPRITTLER, J.E. 2018 Mean-field kinetic theory approach to evaporation of a binary liquid into vacuum. *Phys. Rev. Fluids* **3** (5), 054001.
- FREZZOTTI, A., GIBELLI, L. & LORENZANI, S. 2005 Mean field kinetic theory description of evaporation of a fluid into vacuum. *Phys. Fluids* **17** (1), 012102.
- FREZZOTTI, A. & ROSSI, M. 2012 Slip effects at the vapor–liquid boundary. *AIP Conf. Proc.* **1501** (1), 903–910.

- GAN, Y., XU, A., ZHANG, G. & LI, Y. 2012a Physical modeling of multiphase flow via lattice Boltzmann method: numerical effects, equation of state and boundary conditions. *Front. Phys.* **7** (4), 481–490.
- GAN, Y., XU, A., ZHANG, G., LI, Y. & LI, H. 2011 Phase separation in thermal systems: a lattice Boltzmann study and morphological characterization. *Phys. Rev. E* **84** (4), 046715.
- GAN, Y.B., XU, A.G., ZHANG, G.C., LIN, C.D. & LIU, Z.P. 2019 Nonequilibrium and morphological characterizations of Kelvin–Helmholtz instability in compressible flows. *Front. Phys.* **14** (4), 43602.
- GAN, Y., XU, A., ZHANG, G. & SUCCI, S. 2015 Discrete Boltzmann modeling of multiphase flows: hydrodynamic and thermodynamic non-equilibrium effects. *Soft Matt.* **11** (26), 5336–5345.
- GAN, Y., XU, A., ZHANG, G. & YANG, Y. 2013 Lattice BGK kinetic model for high-speed compressible flows: hydrodynamic and nonequilibrium behaviors. *Europhys. Lett.* **103** (2), 24003.
- GAN, Y., XU, A., ZHANG, G., YU, X. & LI, Y. 2008 Two-dimensional lattice Boltzmann model for compressible flows with high Mach number. *Physica A* **387** (8–9), 1721–1732.
- GAN, Y., XU, A., ZHANG, G., ZHANG, P. & LI, Y. 2012b Lattice Boltzmann study of thermal phase separation: effects of heat conduction, viscosity and Prandtl number. *Europhys. Lett.* **97** (4), 44002.
- GAN, Y., XU, A., ZHANG, G., ZHANG, Y. & SUCCI, S. 2018 Discrete Boltzmann trans-scale modeling of high-speed compressible flows. *Phys. Rev. E* **97** (5), 053312.
- GAO, W. & SUN, Q. 2014 Evaluation of BGK-type models of the Boltzmann equation. *AIP Conf. Proc.* **1628** (1), 84–91.
- GONNELLA, G., LAMURA, A., PISCITELLI, A. & TIRIBOCCHI, A. 2010 Phase separation of binary fluids with dynamic temperature. *Phys. Rev. E* **82** (4), 046302.
- GONNELLA, G., LAMURA, A. & SOFONEA, V. 2007 Lattice Boltzmann simulation of thermal nonideal fluids. *Phys. Rev. E* **76** (3), 036703.
- GONNELLA, G., ORLANDINI, E. & YEOMANS, J.M. 1997 Spinodal decomposition to a lamellar phase: effects of hydrodynamic flow. *Phys. Rev. Lett.* **78** (9), 1695.
- GUNSTENSEN, A.K., ROTHMAN, D.H., ZALESKI, S. & ZANETTI, G. 1991 Lattice Boltzmann model of immiscible fluids. *Phys. Rev. A* **43** (8), 4320–4327.
- GUO, Z. & SHU, C. 2013 *Lattice Boltzmann Method and its Applications in Engineering*. World Scientific Publishing.
- GURTIN, M.E. & VOORHEES, P.W. 1996 The thermodynamics of evolving interfaces far from equilibrium. *Acta Mater.* **44** (1), 235–247.
- HE, X., CHEN, S. & ZHANG, R. 1999 A lattice Boltzmann scheme for incompressible multiphase flow and its application in simulation of Rayleigh–Taylor instability. *J. Comput. Phys.* **152** (2), 642–663.
- HE, Y. & LIN, X. 2020 Numerical analysis and simulations for coupled nonlinear Schrödinger equations based on lattice Boltzmann method. *Appl. Maths Lett.* **106**, 106391.
- HE, Y., LIU, Q., LI, Q. & TAO, W. 2019 Lattice Boltzmann methods for single-phase and solid–liquid phase-change heat transfer in porous media: a review. *Int. J. Heat Mass Transfer* **129**, 160–197.
- HE, B., QIN, C., CHEN, W. & WEN, B. 2022 Numerical simulation of pulmonary airway reopening by the multiphase lattice Boltzmann method. *Comput. Maths Applics.* **108**, 196–205.
- HE, X., SHAN, X. & DOOLEN, G.D. 1998 Discrete Boltzmann equation model for nonideal gases. *Phys. Rev. E* **57** (1), R13–R16.
- HE, Q., TAO, S., YANG, X., LU, W. & HE, Z. 2021 Discrete unified gas kinetic scheme simulation of microflows with complex geometries in Cartesian grid. *Phys. Fluids* **33** (4), 042005.
- HOLWAY, L.H. JR. 1966 New statistical models for kinetic theory: methods of construction. *Phys. Fluids* **9** (9), 1658–1673.
- HU, Y., LI, D. & NIU, X. 2018 Phase-field-based lattice Boltzmann model for multiphase ferrofluid flows. *Phys. Rev. E* **98** (3), 033301.
- HUANG, Q., TIAN, F.B., YOUNG, J. & LAI, J.C.S. 2021a Transition to chaos in a two-sided collapsible channel flow. *J. Fluid Mech.* **926**, A15.
- HUANG, R., WU, H. & ADAMS, N.A. 2021b Mesoscopic lattice Boltzmann modeling of the liquid–vapor phase transition. *Phys. Rev. Lett.* **126** (24), 244501.
- JAENSSON, N. & VERMANT, J. 2018 Tensiometry and rheology of complex interfaces. *Curr. Opin. Colloid Interface Sci.* **37**, 136–150.
- KÄHLER, G., BONELLI, F., GONNELLA, G. & LAMURA, A. 2015 Cavitation inception of a van der Waals fluid at a sack-wall obstacle. *Phys. Fluids* **27** (12), 123307.
- KENDON, V.M., DESPLAT, J.C., BLADON, P. & CATES, M.E. 1999 3D spinodal decomposition in the inertial regime. *Phys. Rev. Lett.* **83** (3), 576.
- LAI, H. & MA, C. 2010 The lattice Boltzmann model for the second-order Benjamin–Ono equations. *J. Stat. Mech.: Theory Exp.* **2010** (4), P04011.

- LAI, H. & MA, C. 2011 Lattice Boltzmann model for generalized nonlinear wave equations. *Phys. Rev. E* **84** (4), 046708.
- LAI, H., XU, A., ZHANG, G., GAN, Y., YING, Y. & SUCCI, S. 2016 Non-equilibrium thermo-hydrodynamic effects on the Rayleigh–Taylor instability in compressible flows. *Phys. Rev. E* **94** (2), 023106.
- LAN, Z.Z., HU, W.Q. & GUO, B.L. 2019 General propagation lattice Boltzmann model for a variable-coefficient compound KdV–Burgers equation. *Appl. Math. Model.* **73**, 695–714.
- LANG, F. & LEIDERER, P. 2006 Liquid–vapour phase transitions at interfaces: sub-nanosecond investigations by monitoring the ejection of thin liquid films. *New J. Phys.* **8** (1), 14.
- LEDESMA-AGUILAR, R., VELLA, D. & YEOMANS, J.M. 2014 Lattice-Boltzmann simulations of droplet evaporation. *Soft Matt.* **10** (41), 8267.
- LI, W., LI, Q., YU, Y. & WEN, Z. 2020 Enhancement of nucleate boiling by combining the effects of surface structure and mixed wettability: a lattice Boltzmann study. *App. Therm. Engng* **180**, 115849.
- LI, Q., LUO, K.H., KANG, Q.J., HE, Y.L., CHEN, Q. & LIU, Q. 2016 Lattice Boltzmann methods for multiphase flow and phase-change heat transfer. *Prog. Energy Combust. Sci.* **52**, 62–105.
- LI, A., LUO, Y.X., LIU, Y., XU, Y.Q., TIAN, F.B. & WANG, Y. 2022 Hydrodynamic behaviors of self-propelled sperms in confined spaces. *Engng Appl. Comput. Fluid Mech.* **16** (1), 141–160.
- LI, Z.H., PENG, A.P., ZHANG, H.X. & YANG, J.Y. 2015 Rarefied gas flow simulations using high-order gas-kinetic unified algorithms for Boltzmann model equations. *Prog. Aerosp. Sci.* **74**, 81–113.
- LI, X., SHI, Y. & SHAN, X. 2019 Temperature-scaled collision process for the high-order lattice Boltzmann model. *Phys. Rev. E* **100** (1), 013301.
- LI, Q., YU, Y., ZHOU, P. & YAN, H.J. 2018 Enhancement of boiling heat transfer using hydrophilic–hydrophobic mixed surfaces: a lattice Boltzmann study. *Appl. Therm. Engng* **132**, 490–499.
- LI, Z.H. & ZHANG, H.X. 2004 Study on gas kinetic unified algorithm for flows from rarefied transition to continuum. *J. Comput. Phys.* **193** (2), 708–738.
- LIANG, H., LI, Y., CHEN, J. & XU, J. 2019 Axisymmetric lattice Boltzmann model for multiphase flows with large density ratio. *Intl J. Heat Mass Transfer* **130**, 1189–1205.
- LIANG, H., LI, Q.X., SHI, B.C. & CHAI, Z.H. 2016a Lattice Boltzmann simulation of three-dimensional Rayleigh–Taylor instability. *Phys. Rev. E* **93** (3), 033113.
- LIANG, H., SHI, B.C. & CHAI, Z.H. 2016b Lattice Boltzmann modeling of three-phase incompressible flows. *Phys. Rev. E* **93** (1), 013308.
- LIANG, H., SHI, B.C., GUO, Z.L. & CHAI, Z.H. 2014 Phase-field-based multiple-relaxation-time lattice Boltzmann model for incompressible multiphase flows. *Phys. Rev. E* **89** (5), 053320.
- LIN, C., LUO, K.H., FEI, L. & SUCCI, S. 2017 A multi-component discrete Boltzmann model for nonequilibrium reactive flows. *Sci. Rep.* **7** (1), 14580.
- LIN, C., LUO, K.H., XU, A., GAN, Y. & LAI, H. 2021 Multiple-relaxation-time discrete Boltzmann modeling of multicomponent mixture with nonequilibrium effects. *Phys. Rev. E* **103** (1), 013305.
- LIN, C., XU, A., ZHANG, G. & LI, Y. 2016 Double-distribution-function discrete Boltzmann model for combustion. *Combust. Flame* **164**, 137–151.
- LIN, C., XU, A., ZHANG, G., LI, Y. & SUCCI, S. 2014 Polar coordinate lattice Boltzmann modeling of compressible flows. *Phys. Rev. E* **89** (1), 013307.
- LIU, H., BA, Y., WU, L., LI, Z., XI, G. & ZHANG, Y. 2018 A hybrid lattice Boltzmann and finite difference method for droplet dynamics with insoluble surfactants. *J. Fluid Mech.* **837**, 381–412.
- LIU, X., CHAI, Z. & SHI, B. 2019 A phase-field-based lattice Boltzmann modeling of two-phase electro-hydrodynamic flows. *Phys. Fluids* **31** (9), 092103.
- LIU, H., KANG, Q., LEONARDI, C.R., SCHMIESCHEK, S., NARVÁEZ, A., JONES, B.D., WILLIAMS, J.R., VALOCCHI, A.J. & HARTING, J. 2016 Multiphase lattice Boltzmann simulations for porous media applications. *Comput. Geosci.* **20** (4), 777–805.
- LIU, F. & SHI, W. 2011 Numerical solutions of two-dimensional Burgers’s equations by lattice Boltzmann method. *Commun. Nonlinear Sci. Numer. Simul.* **16** (1), 150–157.
- LIU, Z., SONG, J., XU, A., ZHANG, Y. & XIE, K. 2022 Discrete Boltzmann modeling of plasma shock wave. In *Proceedings of the Institution of Mechanical Engineers, Part C. Journal of Mechanical Engineering Science*, doi:10.1177/09544062221075943.
- LIU, H., ZHANG, Y., KANG, W., ZHANG, P., DUAN, H. & HE, X.T. 2017 Molecular dynamics simulation of strong shock waves propagating in dense deuterium, taking into consideration effects of excited electrons. *Phys. Rev. E* **95** (2), 023201.
- LIU, H., ZHOU, H., KANG, W., ZHANG, P., DUAN, H., ZHANG, W. & HE, X.T. 2020 Dynamics of bond breaking and formation in polyethylene near shock front. *Phys. Rev. E* **102** (2), 023207.
- LUO, K.H., FEI, L. & WANG, G. 2021 A unified lattice Boltzmann model and application to multiphase flows. *Phil. Trans. R. Soc. A* **379** (2208), 20200397.

- LUO, K.H., XIA, J. & MONACO, E. 2009 Multiscale modeling of multiphase flow with complex interactions. *J. Multiscale Model.* **1** (1), 125–156.
- MAZLOOMI M, A., CHIKATAMARLA, S.S. & KARLIN, I.V. 2015 Entropic lattice Boltzmann method for multiphase flows. *Phys. Rev. Lett.* **114** (17), 174502.
- MILAN, F., BIFERALE, L., SBRAGAGLIA, M. & TOSCHI, F. 2020 Sub-Kolmogorov droplet dynamics in isotropic turbulence using a multiscale lattice Boltzmann scheme. *J. Comput. Sci.* **45**, 101178.
- MONTESSORI, A., PRESTININZI, P., LA ROCCA, M. & SUCCI, S. 2015 Lattice Boltzmann approach for complex nonequilibrium flows. *Phys. Rev. E* **92** (4), 043308.
- MONTESSORI, A., PRESTININZI, P., LA ROCCA, M. & SUCCI, S. 2017 Entropic lattice pseudo-potentials for multiphase flow simulations at high Weber and Reynolds numbers. *Phys. Fluids* **29** (9), 092103.
- MYONG, R.S. 1999 Thermodynamically consistent hydrodynamic computational models for high-Knudsen-number gas flows. *Phys. Fluids* **11** (9), 2788–2802.
- NEGRO, G., CARENZA, L.N., LAMURA, A., TIRIBOCCHI, A. & GONNELLA, G. 2019 Rheology of active polar emulsions: from linear to unidirectional and inviscid flow, and intermittent viscosity. *Soft Matt.* **15** (41), 8251–8265.
- ONUKEI, A. 2002 *Phase Transition Dynamics*. Cambridge University Press.
- ONUKEI, A. 2005 Dynamic van der Waals theory of two-phase fluids in heat flow. *Phys. Rev. Lett.* **94** (5), 054501.
- ONUKEI, A. 2007 Dynamic van der Waals theory. *Phys. Rev. E* **75** (3), 036304.
- OSBORN, W.R., ORLANDINI, E., SWIFT, M.R., YEOMANS, J.M. & BANAVAR, J.R. 1995 Lattice Boltzmann study of hydrodynamic spinodal decomposition. *Phys. Rev. Lett.* **75** (22), 4031.
- OTOMO, H., BOGHOSIAN, B.M. & DUBOIS, F. 2018 Efficient lattice Boltzmann models for the Kuramoto–Sivashinsky equation. *Comput. Fluids* **172**, 683–688.
- PACHALIEVA, A. & WAGNER, A.J. 2021 Connecting lattice Boltzmann methods to physical reality by coarse-graining molecular dynamics simulations. Preprint. [arXiv:2109.05009](https://arxiv.org/abs/2109.05009).
- PARSA, M.R., KIM, C. & WAGNER, A.J. 2021 Nonuniqueness of fluctuating momentum in coarse-grained systems. *Phys. Rev. E* **104** (1), 015304.
- PARSA, M.R. & WAGNER, A.J. 2017 Lattice gas with molecular dynamics collision operator. *Phys. Rev. E* **96** (1), 013314.
- PARSA, M.R. & WAGNER, A.J. 2020 Large fluctuations in nonideal coarse-grained systems. *Phys. Rev. Lett.* **124** (23), 234501.
- PELUSI, F., SBRAGAGLIA, M., BENZI, R., SCAGLIARINI, A., BERNASCHI, M. & SUCCI, S. 2021 Rayleigh–Bénard convection of a model emulsion: anomalous heat-flux fluctuations and finite-size droplet effects. *Soft Matt.* **17** (13), 3709–3721.
- PENG, D.Y. & ROBINSON, D.B. 1976 A new two-constant equation of state. *Ind. Engng Chem. Fundam.* **15** (1), 59–64.
- PERLEKAR, P., BENZI, R., CLERCX, H.J.H., NELSON, D.R. & TOSCHI, F. 2014 Spinodal decomposition in homogeneous and isotropic turbulence. *Phys. Rev. Lett.* **112** (1), 014502.
- PERSAD, A.H. & WARD, C.A. 2016 Expressions for the evaporation and condensation coefficients in the Hertz–Knudsen relation. *Chem. Rev.* **116**, 7727–7767.
- PHILIPPI, P.C., HEGELE, L.A., DOS SANTOS, L.O.E. & SURMAS, R. 2006 From the continuous to the lattice Boltzmann equation: the discretization problem and thermal models. *Phys. Rev. E* **73** (5), 056702.
- QIN, F., DEL CARRO, L., MAZLOOMI MOQADDAM, A., KANG, Q., BRUNSCHWILER, T., DEROME, D. & CARMELIET, J. 2019 Study of non-isothermal liquid evaporation in synthetic micro-pore structures with hybrid lattice Boltzmann model. *J. Fluid Mech.* **866**, 33–60.
- QIU, R., BAO, Y., ZHOU, T., CHE, H., CHEN, R. & YOU, Y. 2020 Study of regular reflection shock waves using a mesoscopic kinetic approach: curvature pattern and effects of viscosity. *Phy. Fluids* **32** (10), 106106.
- QIU, R., ZHOU, T., BAO, Y., ZHOU, K., CHE, H. & YOU, Y. 2021 Mesoscopic kinetic approach for studying nonequilibrium hydrodynamic and thermodynamic effects of shock wave, contact discontinuity, and rarefaction wave in the unsteady shock tube. *Phys. Rev. E* **103** (5), 053113.
- RANA, A.S., SAINI, S., CHAKRABORTY, S., LOCKERBY, D.A. & SPRITTLER, J.E. 2021 Efficient simulation of non-classical liquid–vapour phase-transition flows: a method of fundamental solutions. *J. Fluid Mech.* **919**, A35.
- RASIN, I., MILLER, W. & SUCCI, S. 2005 Phase-field lattice kinetic scheme for the numerical simulation of dendritic growth. *Phys. Rev. E* **72** (6), 066705.
- REDLICH, O. & KWONG, J.N.S. 1949 On the thermodynamics of solutions. V. An equation of state. Fugacities of gaseous solutions. *Chem. Rev.* **44** (1), 233–244.
- REN, Q. 2019 Enhancement of nanoparticle-phase change material melting performance using a sinusoidal heat pipe. *Energy Convers. Manage.* **180**, 784–795.

- ROJAS, R., TAKAKI, T. & OHNO, M. 2015 A phase-field-lattice Boltzmann method for modeling motion and growth of a dendrite for binary alloy solidification in the presence of melt convection. *J. Comput. Phys.* **298**, 29–40.
- RYKOV, V.A. 1975 A model kinetic equation for a gas with rotational degrees of freedom. *Fluid Dyn.* **10** (6), 959–966.
- SAFARI, H., RAHIMIAN, M.H. & KRAFczyk, M. 2014 Consistent simulation of droplet evaporation based on the phase-field multiphase lattice Boltzmann method. *Phys. Rev. E* **90** (3), 033305.
- SBRAGAGLIA, M., BENZI, R., BIFERALE, L., SUCCI, S., SUGIYAMA, K. & TOSCHI, F. 2007 Generalized lattice Boltzmann method with multirange pseudopotential. *Phys. Rev. E* **75** (2), 026702.
- SBRAGAGLIA, M. & SUCCI, S. 2005 Analytical calculation of slip flow in lattice Boltzmann models with kinetic boundary conditions. *Phys. Fluids* **17** (9), 093602.
- SCHWEIZER, M., ÖTTINGER, H.C. & SAVIN, T. 2016 Nonequilibrium thermodynamics of an interface. *Phys. Rev. E* **93** (5), 052803.
- SHAKHOV, E.M. 1968 Generalization of the Krook kinetic relaxation equation. *Fluid Dyn.* **3** (5), 95–96.
- SHAN, X. & CHEN, H. 1993 Lattice Boltzmann model for simulating flows with multiple phases and components. *Phys. Rev. E* **47** (3), 1815–1819.
- SHAN, X. & CHEN, H. 1994 Simulation of nonideal gases and liquid–gas phase transitions by the lattice Boltzmann equation. *Phys. Rev. E* **49** (4), 2941–2948.
- SHAN, X., YUAN, X. & CHEN, H. 2006 Kinetic theory representation of hydrodynamics: a way beyond the Navier–Stokes equation. *J. Fluid Mech.* **550**, 413–441.
- SHI, Y. & SHAN, X. 2021 A multiple-relaxation-time collision model for nonequilibrium flows. *Phys. Fluids* **33** (3), 037134.
- SHI, Y., WU, L. & SHAN, X. 2021 Accuracy of high-order lattice Boltzmann method for non-equilibrium gas flow. *J. Fluid Mech.* **907**, A25.
- SOFONEA, V., BICIUȘCĂ, T., BUSUIOC, S., AMBRUȘ, V.E., GONNELLA, G. & LAMURA, A. 2018 Corner-transport-upwind lattice Boltzmann model for bubble cavitation. *Phys. Rev. E* **97** (2), 023309.
- SOFONEA, V., LAMURA, A., GONNELLA, G. & CRISTEA, A. 2004 Finite-difference lattice Boltzmann model with flux limiters for liquid–vapor systems. *Phys. Rev. E* **70** (4), 046702.
- SOFONEA, V. & SEKERKA, R.F. 2005 Diffuse-reflection boundary conditions for a thermal lattice Boltzmann model in two dimensions: evidence of temperature jump and slip velocity in microchannels. *Phys. Rev. E* **71** (6), 066709.
- STANLEY, H.E. 1971 *Phase Transitions and Critical Phenomena*. Clarendon Press.
- STRUCHTRUP, H. 1997 The BGK-model with velocity-dependent collision frequency. *Contin. Mech. Thermodyn.* **9** (1), 23–31.
- STRUCHTRUP, H. 2005 *Macroscopic Transport Equations for Rarefied Gas Flows: Approximation Methods in Kinetic Theory*. Springer.
- STRUCHTRUP, H., BECKMANN, A., RANA, A.S. & FREZZOTTI, A. 2017 Evaporation boundary conditions for the R13 equations of rarefied gas dynamics. *Phys. Fluids* **29** (9), 092004.
- STRUCHTRUP, H. & FREZZOTTI, A. 2022 Twenty-six moment equations for the Enskog–Vlasov equation. *J. Fluid Mech.* **940**, A40.
- STRUCHTRUP, H. & TORRILHON, M. 2003 Regularization of Grad’s 13 moment equations: derivation and linear analysis. *Phys. Fluids* **15** (9), 2668–2680.
- SU, X. & LIN, C. 2022 Nonequilibrium effects of reactive flow based on gas kinetic theory. *Commun. Theor. Phys.* **74** (3), 035604.
- SUCCI, S. 2001 *The Lattice Boltzmann Equation: For Fluid Dynamics and Beyond*. Oxford University Press.
- SUCCI, S. 2014 A note on the lattice Boltzmann versus finite-difference methods for the numerical solution of the Fisher’s equation. *Intl J. Mod. Phys. C* **25** (01), 1340015.
- SUCCI, S. 2018 *The Lattice Boltzmann Equation: For Complex States of Flowing Matter*. Oxford University Press.
- SUCCI, S., AMATI, G., BONACCORSO, F., LAURICELLA, M., BERNASCHI, M., MONTESSORI, A. & TIRIBOCCHI, A. 2020 Toward exascale design of soft mesoscale materials. *J. Comput. Sci.* **46**, 101175.
- SUCCI, S., MONTESSORI, A., LAURICELLA, M., TIRIBOCCHI, A. & BONACCORSO, F. 2021 Density functional kinetic theory for soft matter. In *Proceedings of SIMAI 2020+21*.
- SUN, D., PAN, S., HAN, Q. & SUN, B. 2016a Numerical simulation of dendritic growth in directional solidification of binary alloys using a lattice Boltzmann scheme. *Intl J. Heat Mass Transfer* **103**, 821–831.
- SUN, D., ZHU, M., WANG, J. & SUN, B. 2016b Lattice Boltzmann modeling of bubble formation and dendritic growth in solidification of binary alloys. *Intl J. Heat Mass Transfer* **94**, 474–487.
- SWIFT, M.R., ORLANDINI, E., OSBORN, W.R. & YEOMANS, J.M. 1996 Lattice Boltzmann simulations of liquid–gas and binary fluid systems. *Phys. Rev. E* **54** (5), 5041–5052.

- SWIFT, M.R., OSBORN, W.R. & YEOMANS, J.M. 1995 Lattice Boltzmann simulation of nonideal fluids. *Phys. Rev. Lett.* **75** (5), 830–833.
- TAVARES, H.S., BIFERALE, L., SBRAGAGLIA, M. & MAILYBAEV, A.A. 2021 Immiscible Rayleigh–Taylor turbulence using mesoscopic lattice Boltzmann algorithms. *Phys. Rev. Fluids* **6** (5), 054606.
- TIAN, Y., *et al.* 2022 Artificial mitochondrion for fast latent heat storage: experimental study and lattice Boltzmann simulation. *Energy* **245**, 123296.
- TORRILHON, M. 2016 Modeling nonequilibrium gas flow based on moment equations. *Annu. Rev. Fluid Mech.* **48**, 429–458.
- TOSCHI, F. & SUCCI, S. 2005 Lattice Boltzmann method at finite Knudsen numbers. *Europhys. Lett.* **69** (4), 549.
- VILAR, J.M.G. & RUBI, J.M. 2001 Thermodynamics ‘beyond’ local equilibrium. *Proc. Natl Acad. Sci.* **98** (20), 11081–11084.
- WAGNER, A.J. 2003 The origin of spurious velocities in lattice Boltzmann. *Intl J. Mod. Phys. C* **17** (1–2), 193–196.
- WAGNER, A.J. 2006 Thermodynamic consistency of liquid–gas lattice Boltzmann simulations. *Phys. Rev. E* **74** (5), 056703.
- WAGNER, A.J. & PAGONABARRAGA, I. 2002 Lees–Edwards boundary conditions for lattice Boltzmann. *J. Stat. Phys.* **107** (1), 521–537.
- WAGNER, A.J., WILSON, L.M. & CATES, M.E. 2003 Role of inertia in two-dimensional deformation and breakdown of a droplet. *Phys. Rev. E* **68** (4), 045301.
- WAGNER, A.J. & YEOMANS, J.M. 1998 Breakdown of scale invariance in the coarsening of phase-separating binary fluids. *Phys. Rev. Lett.* **80** (7), 1429.
- WANG, H. 2017*a* Numerical simulation for the solitary wave of Zakharov–Kuznetsov equation based on lattice Boltzmann method. *Appl. Math. Model.* **45**, 1–13.
- WANG, H. 2017*b* Solitary wave of the Korteweg–de Vries equation based on lattice Boltzmann model with three conservation laws. *Adv. Space Res.* **59** (1), 283–292.
- WANG, H. 2019 Numerical simulation for solitary wave of Klein–Gordon–Zakharov equation based on the lattice Boltzmann model. *Comput. Maths Applics.* **78** (12), 3941–3955.
- WANG, H. 2020 Numerical simulation for (3+1)D solitary wave of extended Zakharov–Kuznetsov equation in dusty plasma based on lattice Boltzmann method. *Phys. Lett. A* **384** (32), 126809.
- WANG, H., LI, X., LI, Y. & GENG, X. 2017 Simulation of phase separation with large component ratio for oil-in-water emulsion in ultrasound field. *Ultrason. Sonochem.* **36**, 101–111.
- WANG, Y., SHU, C., HUANG, H.B. & TEO, C.J. 2015*a* Multiphase lattice Boltzmann flux solver for incompressible multiphase flows with large density ratio. *J. Comput. Phys.* **280**, 404–423.
- WANG, Y., SHU, C. & YANG, L. 2015*b* An improved multiphase lattice Boltzmann flux solver for three-dimensional flows with large density ratio and high Reynolds number. *J. Comput. Phys.* **302**, 41–58.
- WANG, C., XU, A., ZHANG, G. & LI, Y. 2009 Simulating liquid–vapor phase separation under shear with lattice Boltzmann method. *Sci. China, Ser. G* **52** (9), 1337–1344.
- WATARI, M. 2016 Is the lattice Boltzmann method applicable to rarefied gas flows? Comprehensive evaluation of the higher-order models. *J. Fluids Engng* **138** (1), 011202.
- WEEKS, J.D. 1977 Structure and thermodynamics of the liquid–vapor interface. *J. Chem. Phys.* **67** (7), 3106–3121.
- WEI, Y, LI, Y., WANG, Z., YANG, H., ZHU, Z., QIAN, Y. & LUO, K.H. 2022 Small-scale fluctuation and scaling law of mixing in three-dimensional rotating turbulent Rayleigh–Taylor instability. *Phys. Rev. E* **105** (1), 015103.
- WEN, B., ZHAO, L., QIU, W., YE, Y. & SHAN, X. 2020 Chemical-potential multiphase lattice Boltzmann method with superlarge density ratios. *Phys. Rev. E* **102** (1), 013303.
- WEN, B., ZHOU, X., HE, B., ZHANG, C. & FANG, H. 2017 Chemical-potential-based lattice Boltzmann method for nonideal fluids. *Phys. Rev. E* **95** (6), 063305.
- WÖHRWAG, M., SEMPREBON, C., MAZLOOMI MOQADDAM, A., KARLIN, I. & KUSUMAATMAJA, H. 2018 Ternary free-energy entropic lattice Boltzmann model with a high density ratio. *Phys. Rev. Lett.* **120** (23), 234501.
- WU, J.L., LI, Z.H., ZHANG, Z.B. & PENG, A.P. 2021*a* On derivation and verification of a kinetic model for quantum vibrational energy of polyatomic gases in the gas-kinetic unified algorithm. *J. Comput. Phys.* **435**, 109938.
- WU, W., LIU, Q. & WANG, B. 2021*b* Curved surface effect on high-speed droplet impingement. *J. Fluid Mech.* **909**, A7.
- XU, K. 2014 *Direct Modeling for Computational Fluid Dynamics: Construction and Application of Unified Gas-Kinetic Schemes*. World Scientific Publishing.

- XU, A., CHEN, J., SONG, J., CHEN, D. & CHEN, Z. 2021a Progress of discrete Boltzmann study on multiphase complex flows. *Acta Aerodyn. Sin.* **39** (3), 138–169.
- XU, A., GONNELLA, G. & LAMURA, A. 2003 Phase-separating binary fluids under oscillatory shear. *Phys. Rev. E* **67** (5), 056105.
- XU, A., GONNELLA, G. & LAMURA, A. 2004 Numerical study of the ordering properties of lamellar phase. *Physica A* **344** (3–4), 750–756.
- XU, A., SHAN, Y., CHEN, F., GAN, Y. & LIN, C. 2021b Progress of mesoscale modeling and investigation of combustion multi-phase flow. *Acta Aeronaut. Astronaut. Sin.* **42** (12), 625842.
- XU, A., SONG, J., CHEN, F., XIE, K. & YING, Y. 2021c Modeling and analysis methods for complex fields based on phase space. *Chinese J. Comput. Phys.* **38** (6), 631.
- XU, Y.Q., WANG, M.Y., LIU, Q.Y., TANG, X.Y. & TIAN, F.B. 2018b External force-induced focus pattern of a flexible filament in a viscous fluid. *Appl. Math. Model.* **53**, 369–383.
- XU, A.G., ZHANG, G.C., GAN, Y.B., CHEN, F. & YU, X.J. 2012 Lattice Boltzmann modeling and simulation of compressible flows. *Front. Phys.* **7** (5), 582–600.
- XU, A., ZHANG, G. & ZHANG, Y. 2018a Discrete Boltzmann modeling of compressible flows. In *Kinetic Theory*, Chap. 02. (ed. G.Z. Kyzas & A.C. Mitropoulos). InTech.
- YAN, G. 2000 A lattice Boltzmann equation for waves. *J. Comput. Phys.* **161** (1), 61–69.
- YAN, W., CAI, B., LIU, Y. & FU, B. 2012 Effects of wall shear stress and its gradient on tumor cell adhesion in curved microvessels. *Biomech. Model. Mechanobiol.* **11** (5), 641–653.
- YANG, Z., LIU, S., ZHUO, C. & ZHONG, C. 2022b Free-energy-based discrete unified gas kinetic scheme for van der Waals fluid. *Entropy* **24** (9), 1202.
- YANG, Y., SHAN, M., KAN, X., SHANGGUAN, Y. & HAN, Q. 2020 Thermodynamic of collapsing cavitation bubble investigated by pseudopotential and thermal MRT-LBM. *Ultrason. Sonochem.* **62**, 104873.
- YANG, Y., SHAN, M., SU, N., KAN, X., SHANGGUAN, Y. & HAN, Q. 2022a Role of wall temperature on cavitation bubble collapse near a wall investigated using thermal lattice Boltzmann method. *Intl Commun. Heat Mass Transfer* **134**, 105988.
- YANG, L.M., SHU, C., YANG, W.M., CHEN, Z. & DONG, H. 2018 An improved discrete velocity method (DVM) for efficient simulation of flows in all flow regimes. *Phys. Fluids* **30** (6), 062005.
- YANG, Z., ZHONG, C. & ZHUO, C. 2019 Phase-field method based on discrete unified gas-kinetic scheme for large-density-ratio two-phase flows. *Phys. Rev. E* **99** (4), 043302.
- ZANG, D. 2020 *Acoustic Levitation: From Physics to Applications*. Springer Nature.
- ZANG, D., TARAFDAR, S., TARASEVICH, Y.Y., CHOUDHURY, M.D. & DUTTA, T. 2019 Evaporation of a droplet: from physics to applications. *Phys. Rep.* **804**, 1–56.
- ZARGHAMI, A. & VAN DEN AKKER, H.E.A. 2017 Thermohydrodynamics of an evaporating droplet studied using a multiphase lattice Boltzmann method. *Phys. Rev. E* **95** (4), 043310.
- ZHANG, R., HE, X., DOOLEN, G. & CHEN, S. 2001 Surface tension effects on two-dimensional two-phase Kelvin–Helmholtz instabilities. *Adv. Water Res.* **24** (3–4), 461–478.
- ZHANG, R., SHAN, X. & CHEN, H. 2006 Efficient kinetic method for fluid simulation beyond the Navier–Stokes equation. *Phys. Rev. E* **74** (4), 046703.
- ZHANG, Y., XU, A., CHEN, F., LIN, C. & WEI, Z.H. 2022b Non-equilibrium characteristics of mass and heat transfers in the slip flow. *AIP Adv.* **12** (3), 035347.
- ZHANG, Y., XU, A., ZHANG, G., GAN, Y., CHEN, Z. & SUCCI, S. 2019 Entropy production in thermal phase separation: a kinetic-theory approach. *Soft Matt.* **15** (10), 2245–2259.
- ZHANG, D., XU, A., ZHANG, Y., GAN, Y. & LI, Y. 2022a Discrete Boltzmann modeling of high-speed compressible flows with various depths of non-equilibrium. *Phys. Fluids* **34**, 086104.
- ZHANG, D., XU, A., ZHANG, Y. & LI, Y. 2020 Two-fluid discrete Boltzmann model for compressible flows: based on ellipsoidal statistical Bhatnagar–Gross–Krook. *Phys. Fluids* **32** (12), 126110.
- ZHANG, G., XU, A., ZHANG, D., LI, Y., LAI, H. & HU, X. 2021 Delineation of the flow and mixing induced by Rayleigh–Taylor instability through tracers. *Phys. Fluids* **33** (7), 076105.
- ZHANG, Y., XU, A., ZHANG, G., ZHU, C. & LIN, C. 2016 Kinetic modeling of detonation and effects of negative temperature coefficient. *Combust. Flame* **173**, 483–492.
- ZHANG, J. & YAN, G. 2010 Lattice Boltzmann model for the complex Ginzburg–Landau equation. *Phys. Rev. E* **81** (6), 066705.
- ZHANG, J. & YAN, G. 2014 Three-dimensional lattice Boltzmann model for the complex Ginzburg–Landau equation. *J. Sci. Comput.* **60** (3), 660–683.
- ZHANG, J., YAN, G. & DONG, Y. 2009 A new lattice Boltzmann model for the Laplace equation. *Appl. Maths Comput.* **215** (2), 539–547.
- ZHENG, H.W., SHU, C. & CHEW, Y.T. 2006 A lattice Boltzmann model for multiphase flows with large density ratio. *J. Comput. Phys.* **218** (1), 353–371.